Pole Erosion Measurements for the Development Model of the Magnetically Shielded Miniature Hall Thruster (MaSMi-DM)

IEPC-2019-298

Presented at the 36th International Electric Propulsion Conference
University of Vienna • Vienna, Austria
September 15-20, 2019

Robert B. Lobbia,* Ryan W. Conversano,* Alejandro Lopez Ortega,* Sean Reilly,† and Ioannis G. Mikellides‡
Jet Propulsion Laboratory, California Institute of Technology, Pasadena, CA, USA

Magnetically shielded Hall thruster technology reduces channel-wall erosion rates by orders of magnitude to negligible levels with pole cover erosion remaining as one of the main life-limiting components. With suitably thick graphite pole covers for the Development Model Magnetically Shielded Miniature Hall Thruster (MaSMi-DM), a lifetime well in excess of 10 kh is expected before significant amounts of the covers erode. Short duration wear testing of the MaSMi-DM was conducted at each of three operating conditions including 200-W 200-V, 800-W 400-V, and 1000-W 500-V. For each test condition, the inner- and outer-pole cover surface erosion profiles were collected using an optical profilometer. Maximum inner- and outer-pole cover erosion rates were measured during the 200-W condition as 53 µm/kh and 47 µm/kh respectively, suggesting a lifetime of 28 kh until full erosion of the covers at this worst-case—highest amplitude discharge oscillation—condition. For the 800-W and 1000-W conditions, outer-pole erosion was nearly negligible (<16 µm/kh) while inner-pole erosion was <30 µm/kh. Numerical simulations of the MaSMi-DM pole cover erosion rates agree well (mostly within a factor of 2) with the short-duration wear testing and these simulations indicate that both low-energy ions and beam ions originating near the corners of the discharge channel are the erosive sources. Throughout the first short-duration wear test segment at 1000-W, a 54°C increase in inner magnetic coil steady-state temperature occurred in the first 330-h of total thruster operation that is believed to have originated from the fuller outgassing of the thruster components as well as the subtle creep of internal fasteners expected at the elevated temperature condition. All other thruster telemetry remained invariant for the duration of each test segment indicating minimal thruster changes occurred throughout this campaign adding confidence to the thruster design goal of ≥100 kg-Xe throughput with ≥10 kh life.

I. Introduction

Magnetic shielding of Hall thrusters enables thruster lifetimes greater than 10-kh and has been successfully implemented on several laboratory model thrusters including the H6MS [1,2], HERMeS (Hall Effect Rocket with Magnetic Shielding) [3,4], H9 [5,6], MaSMi [7–9], and others. In all implementations of magnetic shielding to date, discharge channel wall erosion is largely eliminated but pole surface erosion remains, albeit at

* Staff Engineer, Electric Propulsion Group
† Staff Engineer, Thermal Engineering Group
‡ Principal Engineer, Electric Propulsion Group

manageable levels that still allow for Hall thruster lifetimes in the 10's of kilohours. While numerical models of pole erosion exist [10,11], they are not yet of sufficient fidelity to predict pole erosion without gound testing. Thus, to qualify a magnetically shielded thruster for long lifetimes, short and long duration wear tests are required. The NASA GRC and JPL developed HERMeS Technology Development Unit (TDU) thrusters are 12.5 kW magnetically-shielded Hall thrusters designed for lifetimes of 50 kh that have completed a series of short-duration wear tests to assess pole erosion [12–15]. These TDU pole erosion studies quantified rates of pole erosion for both carbon graphite and molybdenum pole covers as high as 120 μm/kh and 1450 μm/kh respectively. Pole erosion experiments first performed with the H6MS [16] and later with the TDU thrusters are now considered an essential step to correctly size the thickness of the pole covers on a magnetically shielded thruster to meet a given lifetime requirement. These early pole erosion experiments also identified a very wide variance in the rates of pole erosion both as functions of radial location on the pole cover and on the thruster operating condition. Zeroth order initial estimates of pole erosion suggested that the higher power conditions would generate greater erosion (more discharge current = more ions and higher discharge voltage = more energetic ions impacting the poles). However, the largest erosion rates were observed at an off-nominal lower-current operating condition for the TDU at 600-V 6-kW [13]. At this condition, discharge oscillations were relatively large and recent numerical work has shown the important role discharge dynamics can have on affecting the pole erosion rates [10,11].

The MaSMi-DM thruster (see Figure 1) is a part of the Jet Propulsion Laboratory's (JPL) Ascendant Sub-kW Transcelestial Electric Propulsion System (ASTRAEUS) program that is developing an in-space electric propulsion system for SmallSat high-ΔV interplanetary exploration. A full overview of the ASTREAUS program is provided in Ref. [17]. The ASTREAUS program is on track to deliver by mid-2021 the TRL-6 development of: a low-power Hall thruster (MaSMi), an ultra-compact power processing unit (PPU), a xenon flow controller (XFC) using commercially available flight-demonstrated parts, and a commercial off-the-shelf (COTS) gimbal. JPL has selected the commercial partner Apollo Fusion, Inc. to co-develop and fabricate ASTRAEUS hardware including the thruster Engineering Model, MaSMi-EM. The MaSMi-DM thruster was fabricated by JPL in 2017 to provide a performance and lifetime baseline for MaSMi-EM and the later flight versions as the DM unit retains the same plasma wetting thruster dimensions and magnetic field topology. Detailed performance measurements, characterizations, and laser-induced fluorescence measurements of the MaSMi-DM thruster are available in Refs. [18,19].

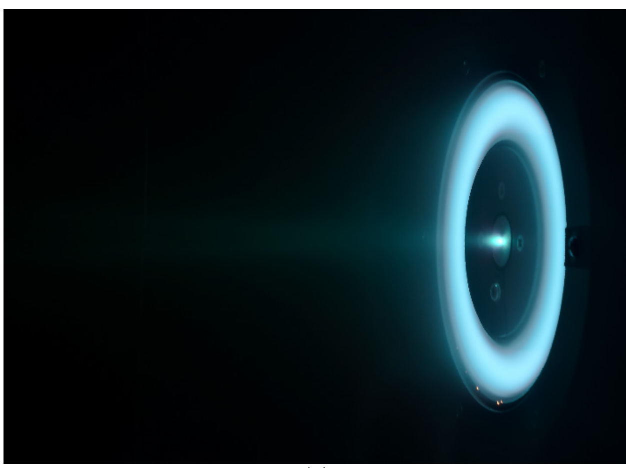

(a)

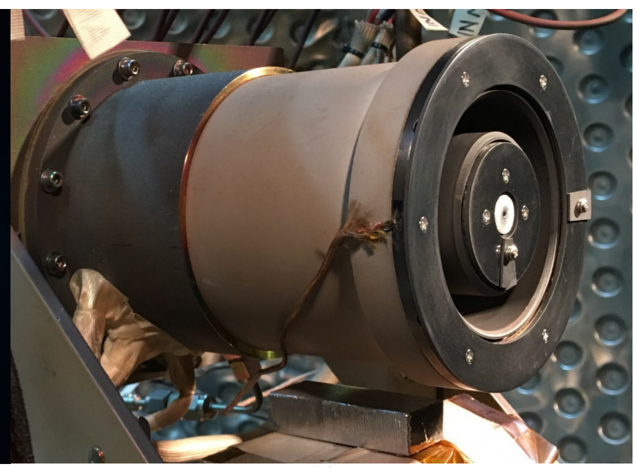

(b)

Figure 1. (a) MaSMi-DM thruster running at 200-W 200-V during pole erosion test campaign. Inner pole cover mask is located at 6:00 while outer is at 3:00. (b) MaSMi-DM thruster on thrust stand in JPL Highbay facility showing masked regions more clearly.

II. Setup and Approach

Three short duration wear test segments were conducted for this effort at 200-V 1-A, 400-V 2-A, and 500-V 2-A in the JPL Highbay vacuum test facility from November 2018 to January 2019. The details of the test setup and diagnostics are provided in the following sections.

A. Highbay vacuum test facility

The JPL Highbay vacuum test facility is a 5.2 m long, 2.6 m diameter cylindrical cryogenically pumped chamber. Three cryopumps provide a nominal pumping speed of 40 kl-Xe/s with a base pressure of $<1\times10^{-7}$ torr-Xe and a maximum flow (200 V 4 A condition) operational pressure of ≤1.1×10^{-5} torr-Xe. These pressures are collected by two Stabil-Ion gauges calibrated for Xe with one located axially at the exit plane and radially at the mid-point from the thruster edge to the chamber wall as shown in Figure 2(a) in compliance with the electric propulsion standard practice [20]. A chevroned graphite beam dump and graphite lined walls, Figure 2(b), are used to minimize backsputtered material.

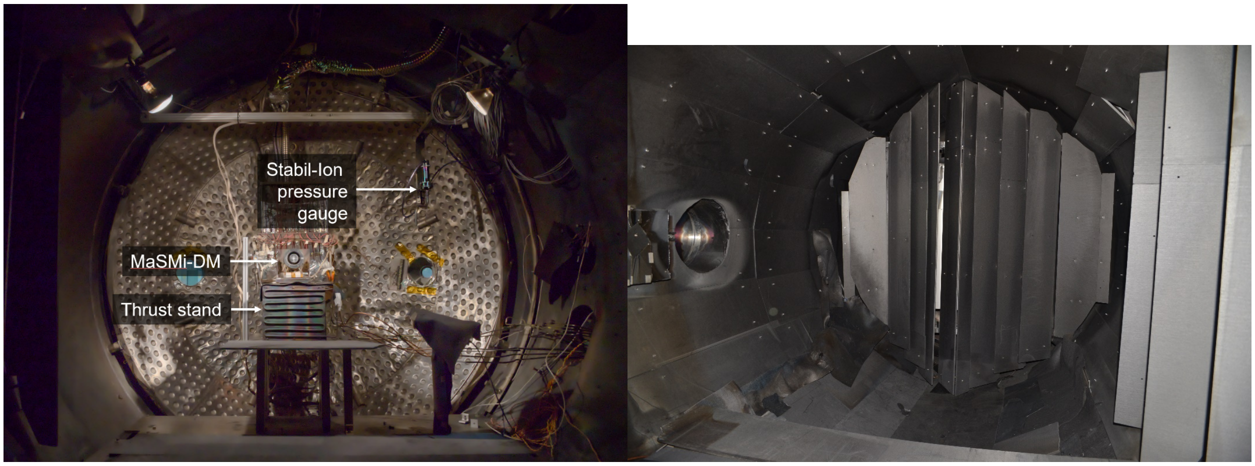

(a) (b)

Figure 2. (a) Photo of MaSMi-DM on thrust stand with location of pressure gauge. (b) Photo of chevroned graphite beam dump and graphite lined walls.

B. Test setup

A top-level overview of the pole-erosion test campaign setup in the Highbay chamber is presented in Figure 3. Locations of the cryopumps, pressure gauges, QCM, cameras, LN_2 shrouds, and beam dump are all indicated. One camera was connected to a digital video recording (DVR) system that continually recorded thruster operation.

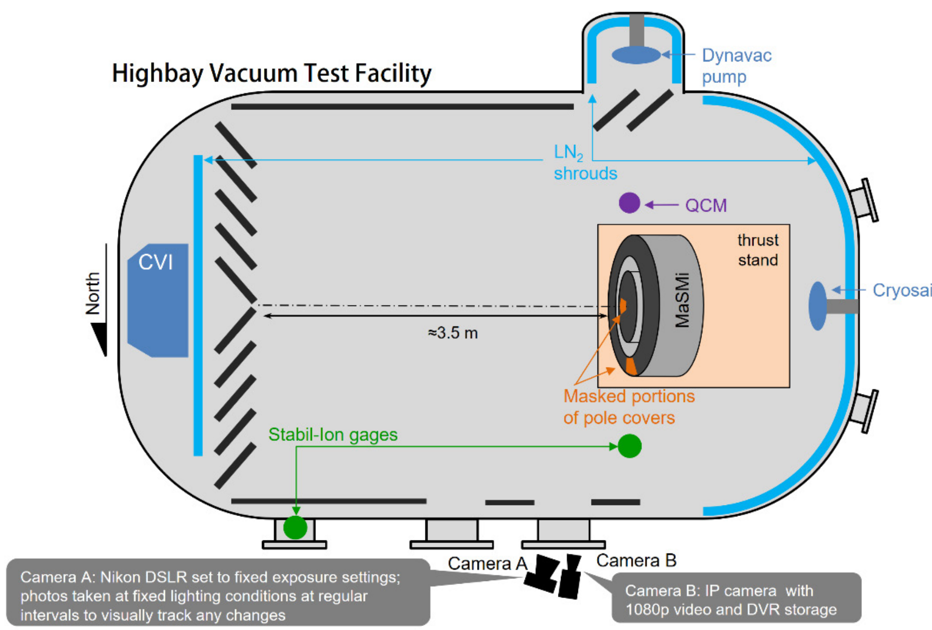

Figure 3. Top view of test setup in the Highbay chamber (not drawn to scale).

The thruster power was provided from a series of laboratory DC power supplies with Figure 4 illustrating the configuration for the discharge power filter, high-speed voltage and current probes, as well as thruster harnessing.

New harnessing was developed for this campaign that included a series of 4 parallel shielded twisted pair (STP, 12 AWG) cables to reduce the cabling inductance to values of 1-2 μH typical of flight-like cable lengths.

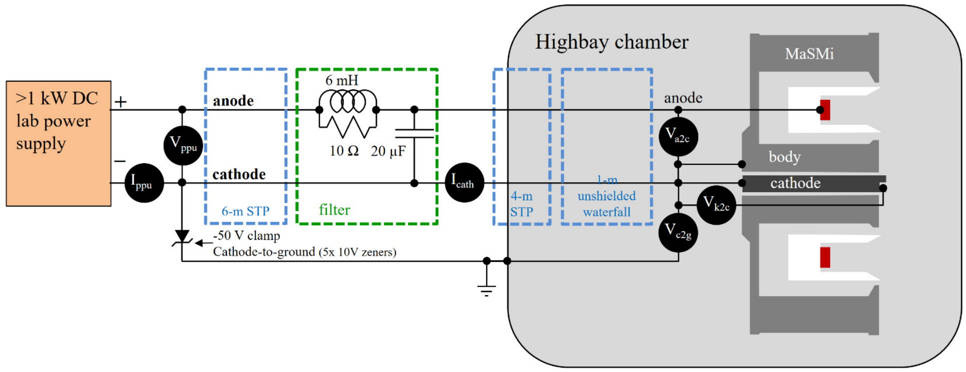

Figure 4. Electrical configuration of the thruster (not drawn to scale).

Two APEX mass flow controllers (MFCs) were used to control the anode and cathode xenon (with 99.999% purity) flow to the thruster. These MFCs were calibrated in-house to <±1% uncertainty using BIOS DryCal systems.

C. Thruster control software interface

The thruster was controlled via a newly developed LabVIEW based interface through digital links to all the power supplies and MFCs. This main thruster control interface also continuously collected and logged telemetry from a slow (2.5 Hz) data acquisition (DAQ) system, a high-speed (100 MHz) 8-channel oscilloscope, and various other diagnostics (78 total channels). The control software also provided the capability to run the thruster unattended with multiple fault monitoring channels, interlocks, and watchdogs that safe the system (shutdown the thruster) and alert the operators (via email and text messages) when a fault occurred.

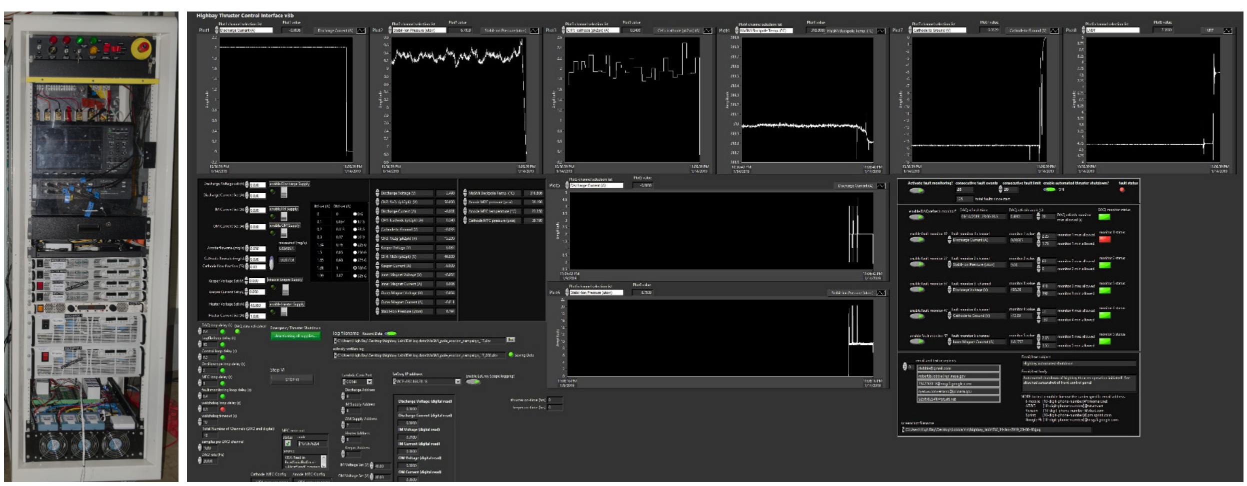

(a) (b)

Figure 5. (a) Photo of rack containing all thruster power supplies, DAQ, oscilloscope, shunts, and voltage dividers. (b) Screenshot of thruster control software that enabled unattended thruster operations for the longer duration test segments.

D. Low-speed and high-speed thruster telemetry

An optically isolated set of 24x 16-bit DAQ channels were used to collect a variety of thruster signals as listed in Table 1. These signals were each acquired through sense lines using calibrated voltage dividers and shunts. Additional low-speed telemetry was sampled from each of the digitally linked DC power supplies and the MFCs. The low-speed analog signals were sampled at 2500 Hz and 1000 samples were averaged for each measurement providing the effective datarate of 2.5 Hz. The thruster was instrumented with a total of 3 type-K thermocouples

(TCs): (1) backpole, (2) front outer pole, and (3) inner coil. Only the backpole TC was recorded in the DAQ logfile with all remaining TCs (including thrust stand and QCM TCs) written down in a manual spreadsheet log by the thruster operators.

Table 1. Low-speed optically isolated telemetry channels.

Channel	Channel	Channel
Outer magnet voltage and current	MaSMi-DM backpole temperature	Thrust stand LVDT
Inner magnet voltage and current	Stabil-Ion gauge pressure	Thrust stand tilt
Cathode keeper voltage and current	Convectron gauge pressure	Anode flowrate (digital)
Discharge voltage and current	Cathode-to-ground voltage	Cathode flowrate (digital)

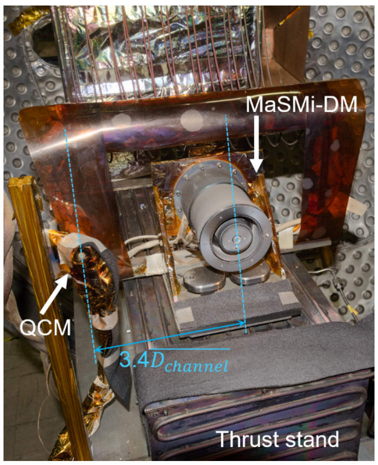

Figure 6. Photograph showing proximity of QCM to thruster.

An 8-channel 12-bit LeCroy HDO8038A oscilloscope was used to capture high-speed signal waveforms as well as signal statistics. Four wideband high-voltage active differential voltage probes (Pico TA04X, DC-70 MHz) were used to measure the discharge power supply output voltage (labeled "PPU"; before filter), the anode to cathode voltage (using sensing lines at thruster), the keeper to cathode voltage, and the cathode to ground voltage. Two wideband current transformers (Pearson 110, 1 Hz – 20 MHz) were used to measure the discharge power supply output current (labeled "PPU"; before filter) and the cathode current (after the filter). While the signal statistics were logged continuously every second, full waveform captures (with 50M samples per channel) were manually collected intermittently throughout each segment.

E. Quartz crystal microbalance

An Inficon XTM/2 quartz crystal microbalance (QCM) was setup with water cooling and radiation shielding in close proximity ($3.4\overline{D_{channel}}$ radially off-axis, where $\overline{D_{channel}}$ is the mean channel diameter) to the MaSMi-DM as shown in Figure 6. A new resonant plate was added at the start of the test segments and a TC was added to monitor the QCM temperature.

F. Thrust stand

A water cooled inverted pendulum thrust stand was used in displacement mode to measure the thrust periodically throughout this test campaign in compliance with electric propulsion thrust measurement standard practices [21]. An inclinometer and tilt control motor were utilized to maintain constant inclination during thrust measurements and calibrations. Calibrations were performed immediately following each thrust measurement by lowering a series of known masses that applied up to 70 mN of calibration force to the thruster via a pulley system. This thrust stand has been carefully tuned to low-thrust operation and has demonstrated repeatability to ±0.1 mN and an overall accuracy of approximately ±1% [18]. Six TCs distributed around the thrust stand were used to ensure the thrust stand and all major elements remained in thermal equilibrium.

G. Profilometer and pole covers

A Nanovea ST400 non-contact white-light chromatic confocal optical profilometer, previously used by Sekerak on the H6MS [16], was used to measure pole surface features. A narrow focus optic with 1.1 mm total range was used with ±0.2 μm height accuracy and vertical static noise of ±1.7 nm. A series of x, y, and θ positioning stages were used to move the sample through a desired set of coordinates. A special fixture was fabricated for the profilometer scanning platform that allowed for precision mounting of pole cover samples in a repeatable manner using mounting screws tightened to consistent torques (see Figure 7). Typical scan settings used r-θ maps with a radial resolution of 1 μm and θ resolution of 0.2° that required approximately 2 days to complete.

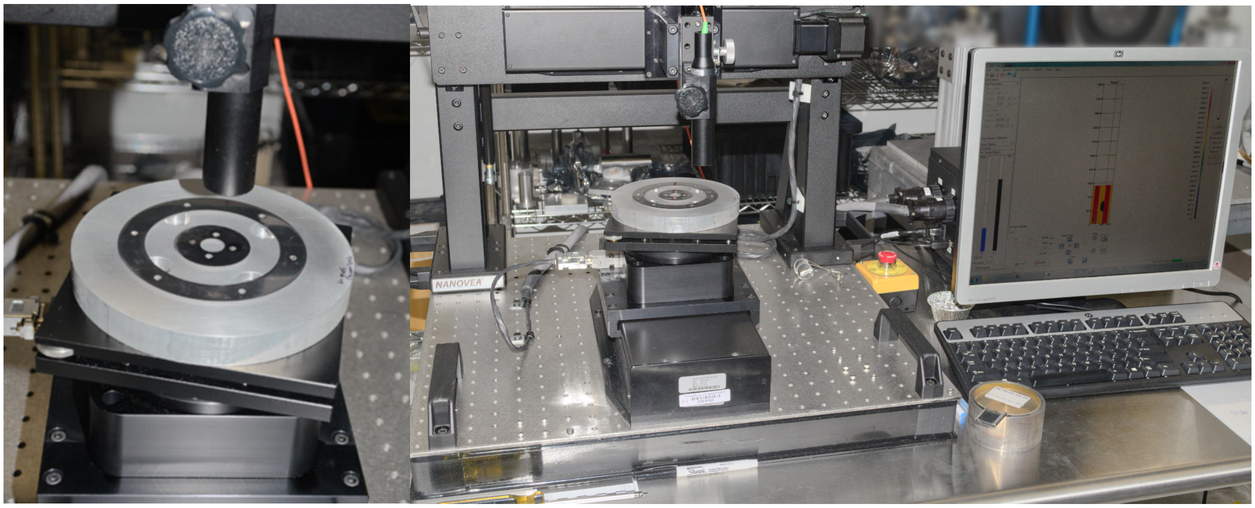

(a) (b)

Figure 7. (a) Close-up and (b) zoomed-out views of profilometer setup during scan of pre-test pole cover set.

A total of six sets of polished pole covers were fabricated for this test campaign and the best (i.e. highest degree of polish) three were selected so that each test segment began with a new pole cover set. A computer aided design (CAD) rendering of a graphite pole cover set with the graphite mask wedges is shown in Figure 8(a). The graphite material impurities were < 200 PPM and after fabrication and polishing, the pole covers and masks were cleaned in a sonic bath, and then baked out in a vacuum furnace. The pole cover thicknesses were 1.5 mm while the mask wedges were 0.65 mm thick. The 1.5 mm thick graphite material was deemed sufficient to meet the 10 kh lifetime goal for MaSMi while the thinner masks were used to minimize perturbing the local area where the erosion-step-height change measurements were performed, while still retaining sufficient thickness for survival of the short duration wear segments and user handling and installation. The same stainless steel fasteners were used for all test segments and since these were not expected to last 10 kh, fastener design modifications have already been made for the ASTREAUS MaSMi-EM version that exceed this lifetime requirement.

For each set of pole covers, pre-post and post-test profilometry scans were performed. The pre-test polished graphite surface was shown to be exceptionally smooth locally to within ±1 μm. Global waviness was observed across the entire pole cover surfaces that measured approximately ±20 μm and ±40 μm for the inner and outer pole covers respectively. These larger scale variations are a result of fabrication and mounting tolerances. The method of analysis used in this test campaign involves subtracting out this pre-test scan from the post-test scan to eliminate the waviness from the data. Also, since only local step-change heights are used in the measurement of erosion, only the local flatness is relevant to the uncertainty, thus total erosion rate uncertainty is estimated according to Eq. (1).

$$\delta\dot{h}_{erosion} \approx \Delta t^{-1}\sqrt{(\pm 1\ \mu m)^2 + (\pm 0.2\ \mu m)^2} \tag{1}$$

This equation includes the segment duration runtime, Δt, and for the three conditions run during this campaign, the approximate erosion rate uncertainties are estimated in Eq. (2).

$$\delta\dot{h}_{erosion} \approx \begin{cases} \pm 4\,\frac{\mu m}{kh},\ \text{200-V 1-A} \\ \pm 5\,\frac{\mu m}{kh},\ \text{400-V 2-A} \\ \pm 8\,\frac{\mu m}{kh},\ \text{500-V 2-A} \end{cases} \tag{2}$$

These erosion rate uncertainties are comparable to—but slightly lower than—those seen with TDU wear testing [22] of similar segment durations owing to the use to a closer focusing optic (with finer resolution) and an improved level correcting method.

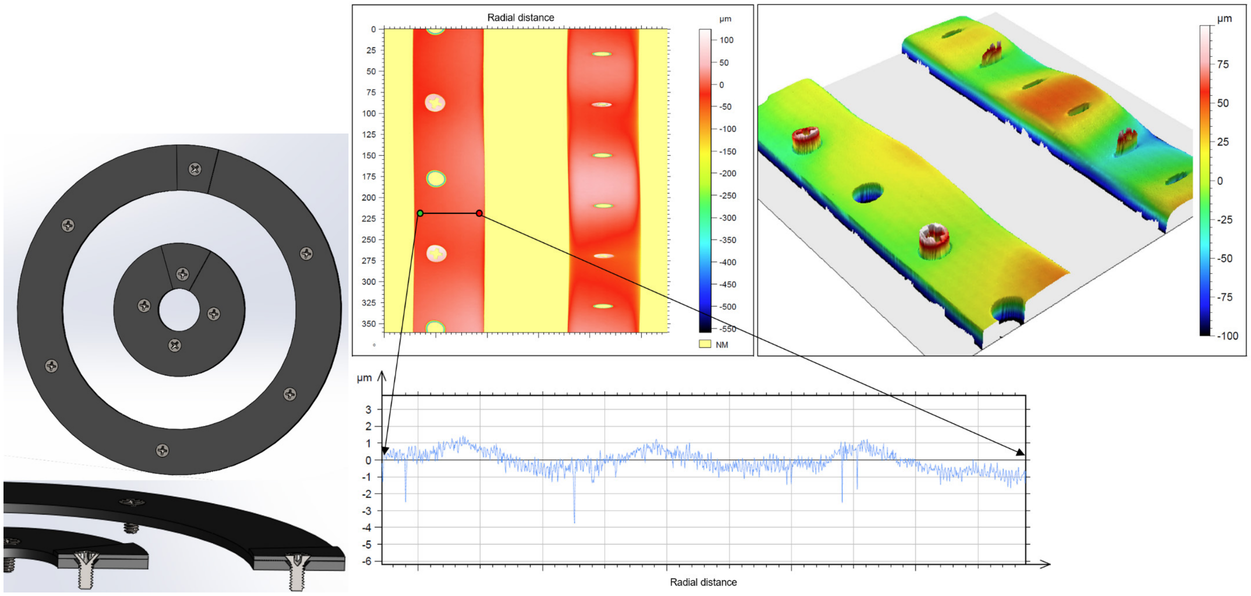

Figure 8. (a) CAD rendering of pole covers and masks. (b) Surface flatness analysis of pre-test pole cover set (in r-θ coordinates) showing graphite pole cover surface local flatness to ±1 µm and pre-leveling global waviness to ±30 µm.

H. Test sequence

Figure 9 presents the testing sequence used during this test campaign. Each short duration wear segment was expected to last approximately 20 days including a few days of overlap with the following segment.

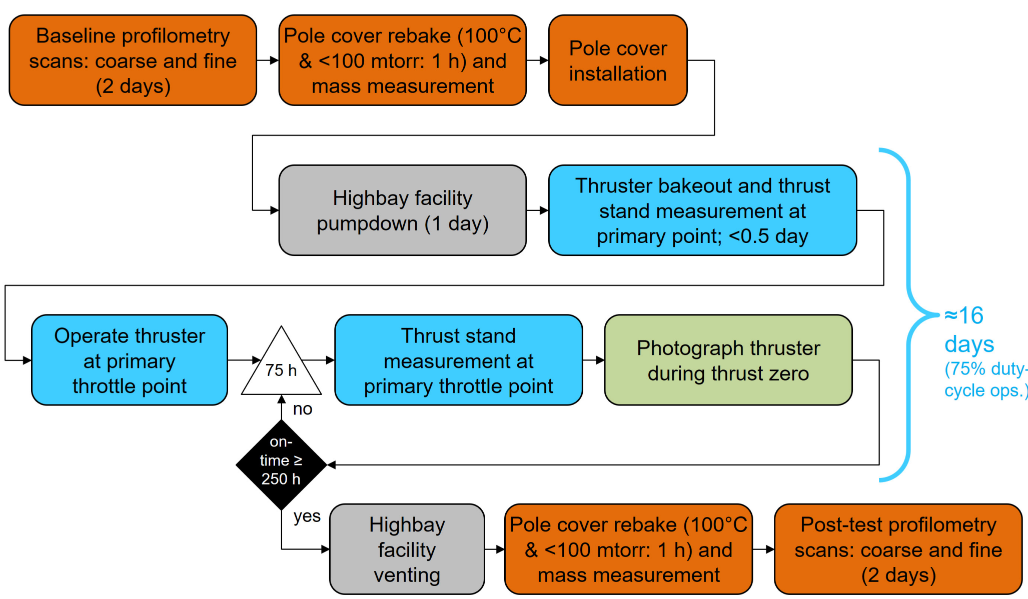

Figure 9. Top view of test setup in the Highbay chamber (not drawn to scale).

Following a baseline pre-test profilometry scan the sample was vacuum (< 100 mtorr) baked at 100°C[§] for one hour to remove water and other absorbed volatiles to enable accurate and consistent mass measurements accurate to ±0.4 mg.[**] The covers were then installed on the thruster along with the graphite mask wedges (as seen in Figure 1) and the facility was pumped down to high vacuum. After a thruster bakeout, an initial thrust measurement was performed (thruster was powered off briefly to obtain an accurate "zero"). The thruster was then run continuously for 75 hours at which point another thrust measurement was obtained. Thrust measurements were repeated every 75 h until a total runtime of 250 h was attained or until the segment was voluntarily concluded. Once the segment runtime was completed, the chamber was vented and the pole covers removed for re-baking, re-massing and profilometry scanning. The loss in mass expected from the covered was expected to enable a global average estimate of the erosion rate for the inner and outer pole covers that could be compared to the radially resolved rates from the profilometry scans.

III. Results

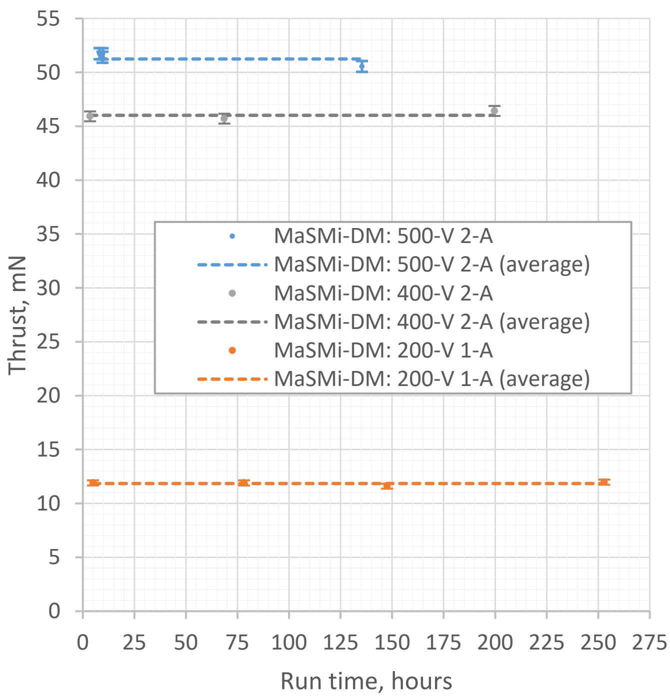

Figure 10. Invariance in thrust throughout duration of all three short duration wear segments.

A. Thruster performance throughout segments

Thruster telemetry and performance data was collected throughout each of the short duration wear segments to confirm invariance in thruster operation during these tests. Figure 10 presents the lack of any appreciable thrust changes throughout the three segments: 500-V 2-A (136 h total runtime), 400-V 2-A (213 h total runtime), and 200-V 1-A (253 h total runtime). Since the thrust vs time remains approximately within the uncertainty (error bars are included but barely exceed the data-point marker size) for all segments, the thruster performance is therefore invariant throughout these durations. Thrusters not designed with magnetic shielding at beginning of life are known to exhibit a loss in performance during the first few hundred hours of operation [23], but this was not observed with the magnetically shielded design of MaSMi because the discharge chamber does not erode. The thruster total efficiency and specific impulse also exhibited invariance outside of the uncertainty for each segment.

B. Thruster characteristics and telemetry throughout segments

Thruster telemetry signals during the 200-V 1-A segment also remained roughly invariant as shown in the timestamped history of Figure 11. Figure 12 plots these same data as a function of thruster on-time which totaled 253 hours. There were 6 thruster shutdowns during this segment that included 4 shutdowns for thrust measurements and two fault monitor automated shutdowns due to brief facility pressure spikes. Plotting the data versus on-time eliminates the temporal gaps when the thruster was inactive, but it does not eliminate the spikes in the various signals as the thruster is shutdown and restarted. The heaterless cathode ignition procedure requires significant cathode flow (comparable to the anode flow) that roughly doubles the facility pressure for a couple

[§] Technically, the pole covers were already vacuum baked at much higher temperatures. This step was performed immediately (< 1 hour) before massing the covers to obtain a consistent "dry" mass measurement. The covers were transported to the scale in sealed bags packed with desiccant.

[**] This accuracy was verified by comparing the masses of spare non-eroded pole covers included in the baked batches.

minutes at most when restarting the cathode and thruster leading to pressure spikes with each ignition. The discharge signals (voltage, current, and power) also undergo brief spikes during this ignition procedure. Spark events were not observed during the 200-V 1-A segment, but more than a dozen current dropouts were observed that the high-speed oscilloscope telemetry, "CH1: Icathode (pk2pk) (A)," picked up. These dropouts were rather brief, typically lasting 10-50 μs, and the continuous operation of the cathode keeper at a low-level discharge (0.2 A) likely helped keep the thruster lit during these current dropout events. It was surmised during operation that these events might have been the result of internal intermittent Paschen breakdown arising from a known internal fabrication issue in the development model thruster that left a small unintended hairline gap in the base of the anode. An attempt was made to plug this gap with fiberglass filler which appeared initially successful throughout the performance characterization [18] and LIF [19] campaigns that preceded this pole erosion test campaign. However, this fiberglass filler may have deteriorated after 200-300 hours of total thruster operation time. A post-test thruster disassembly confirmed this hypothesis with the observation of plasma ablated material in the region of the gap. The issue that resulted in this gap has been eliminated in the design of the MaSMi-EM thruster.

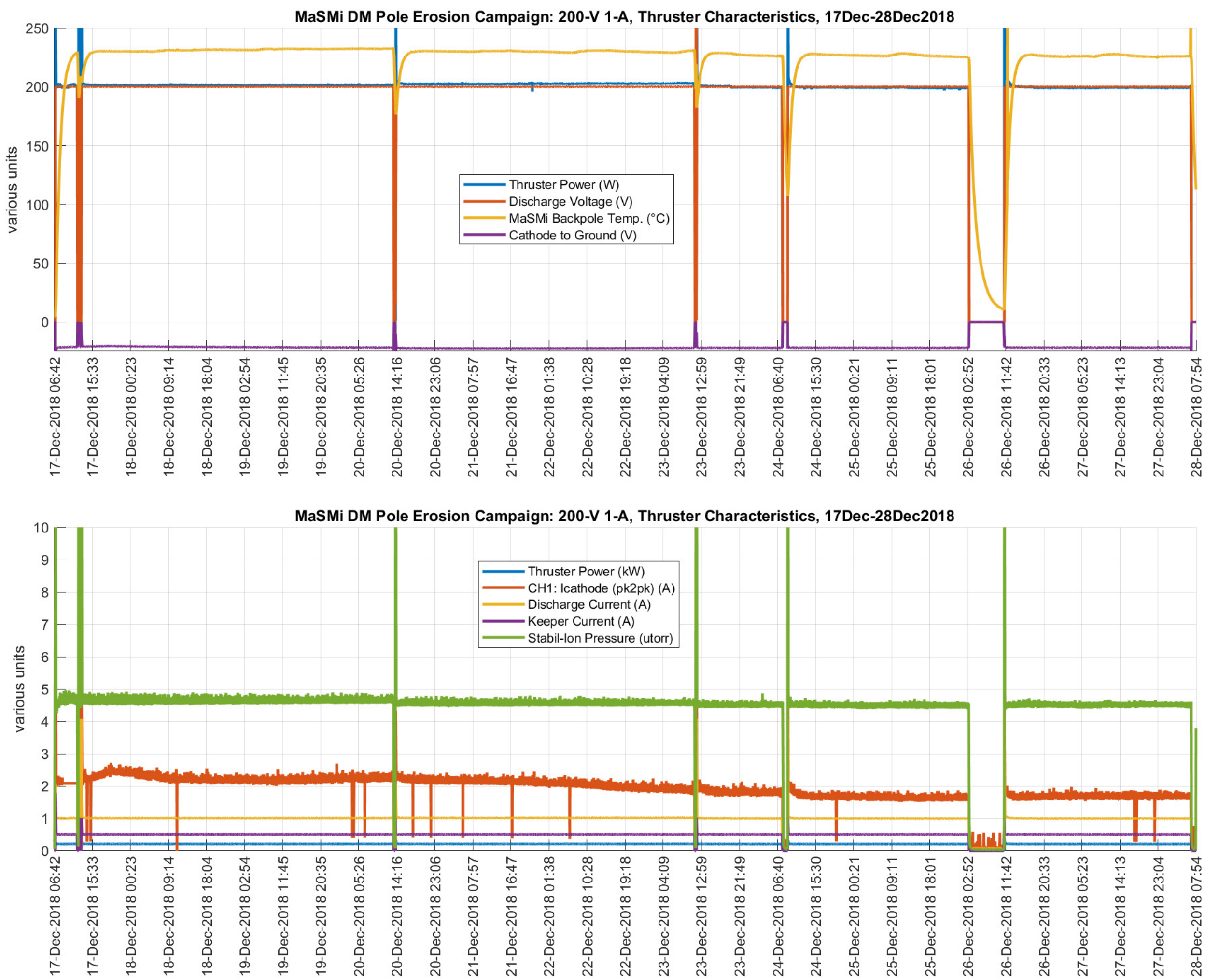

Figure 11. Time history plots of various thruster telemetry for the 200-V 1-A short duration wear segment.

The steady-state thruster backpole temperature experienced a slight decrease throughout the segment from an initial 233°C to 226°C by the conclusion of the segment. Small scale oscillations of ±1.5°C were also observed (with periods of tens of hours) during in the steady-state backpole temperate. Since the accuracy of this type-K thermocouple was ±2.2°C these oscillations are within the uncertainty. The 6.4°C drop in the steady-state backpole temperature is just outside the uncertainty and the source for this change is unknown. As shall be discussed in a following section, this 200-V 1-A condition led to the greatest amount of pole erosion so it is plausible that the emissivity increased as the pole covered transitioned from a mirror-like polished surface (<±1 μm roughness) to a matte surface (with upwards of 13.4 μm total erosion). Increased pole cover emissivity could have contributed to the observed backpole steady-state temperature decrease [24].

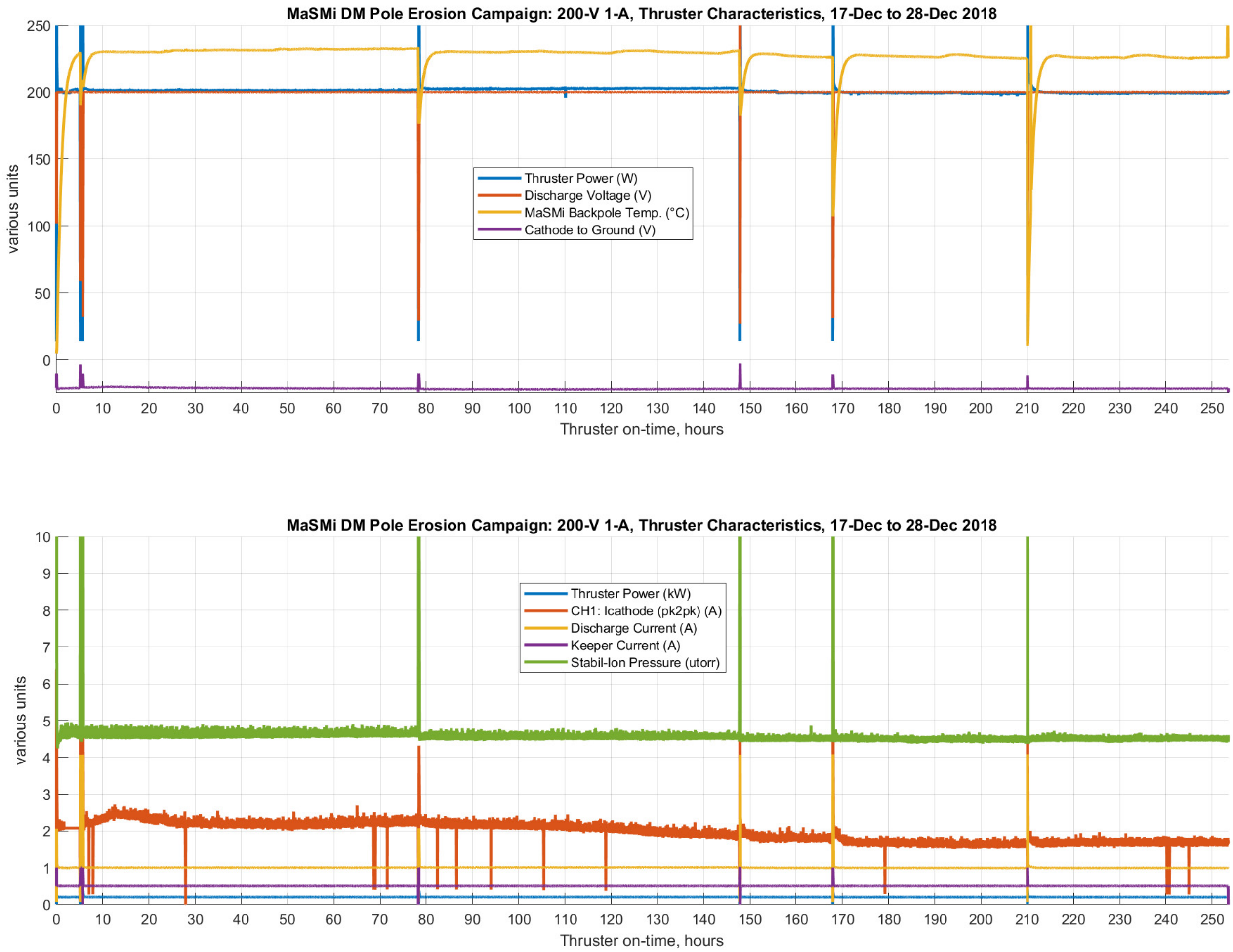

Figure 12. Various thruster telemetry signals versus thruster on-time for the 200-V 1-A short duration wear segment.

The discharge current oscillation amplitude also experienced a slight decrease during the 200-V 1-A segment. The initial cathode current peak-to-peak amplitude rose to 2.5 A_{pk2pk} (at 14 hours into the segment) then gradually lessened to 1.7 A_{pk2pk} around 180 hours and remained at that level for the duration of the 253 hour segment. It is not known why the thruster oscillation amplitude decreased by 32% during the segment. Since the discharge channel walls are slowly being coated in backsputtered graphite it is plausible this could have an effect. Oscillation amplitude changes of this order of magnitude have been observed before as magnetically shielded thrusters accumulate backsputtered graphite [25].

Thruster telemetry throughout the 400-V 2-A (800 W) segment is presented next in Figure 13. Unlike the 200-V 1-A condition, all steady-state signals are stable during the entire 213 hour segment. This segment did however experience many more unexpected thruster shutdowns (29 total) that occurred during large current dropouts likely caused by the Paschen breakdown issues discussed earlier. This higher power 800 W condition led to a hotter steady state backpole temperature of 320°C that, when coupled with the larger anode flowrate and discharge voltage, likely resulted in more optimal Paschen breakdown conditions in the region of the known fabrication flaw. While the keeper was operated at a low level during this entire segment, it was unable to keep the thruster lit during these current dropouts since the thruster magnetic field (which remained on during these events) limited sufficient electron flow to the discharge.

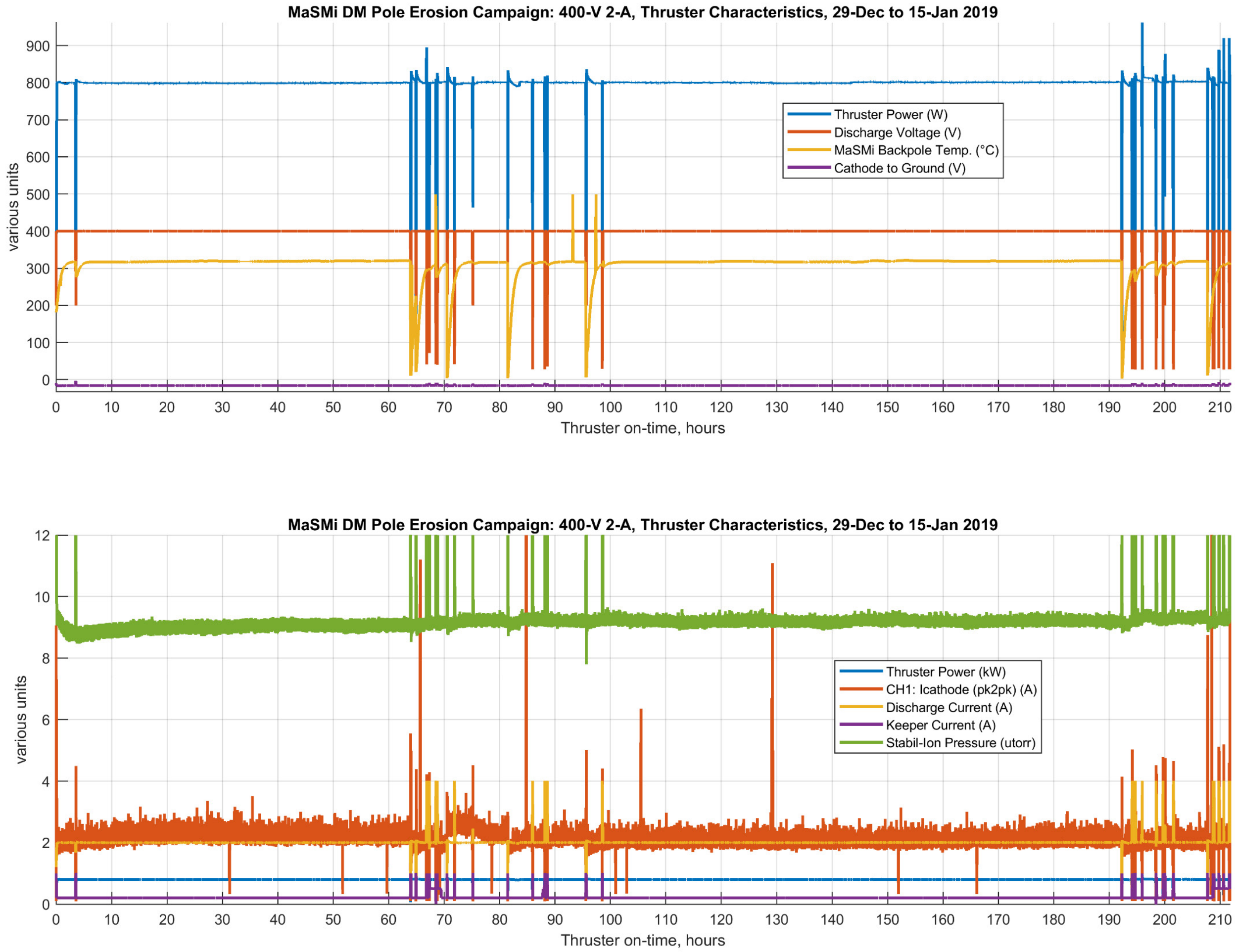

Figure 13. Various thruster telemetry signals versus thruster on-time for the 400-V 2-A short duration wear segment.

Thruster telemetry versus on-time for the highest power short duration wear segment, 500-V 2-A, is presented in Figure 14. The telemetry for the initial 75 hours of this segment was recorded by hand only as the DAQ system was offline during this time. These hand entries were made only every 3 hours and lead to considerable granularity in the data. While this case is presented last, it was the first segment run and initially the cathode keeper was not operated continuously. At a runtime of 57 hours, the keeper was activated and remained on for the duration of this and all subsequent segments[††]. This continuous operation of the keeper appeared to limit (but not eliminate) the occurrence of unexpected thruster shutdowns due to current dropouts as discussed previously. The high-speed cathode current signal also captured a number of discharge current oscillation spikes (brief excursions above 4 A_{pk2pk} in discharge current) for both this 500-V 2-A segment as well as the previously discussed 400-V 2-A segment. However these transient increases in oscillation all occurred during thruster startups as the power and voltage were throttled up. Thus, these are not "spark"-like events that are known to occur with magnetically shielded thrusters as back-sputtered carbon detaches from the thruster and vaporizes in biased gaps or in the main plasma discharge [25].

[††] The keeper was only turned off right before performing thrust measurements.

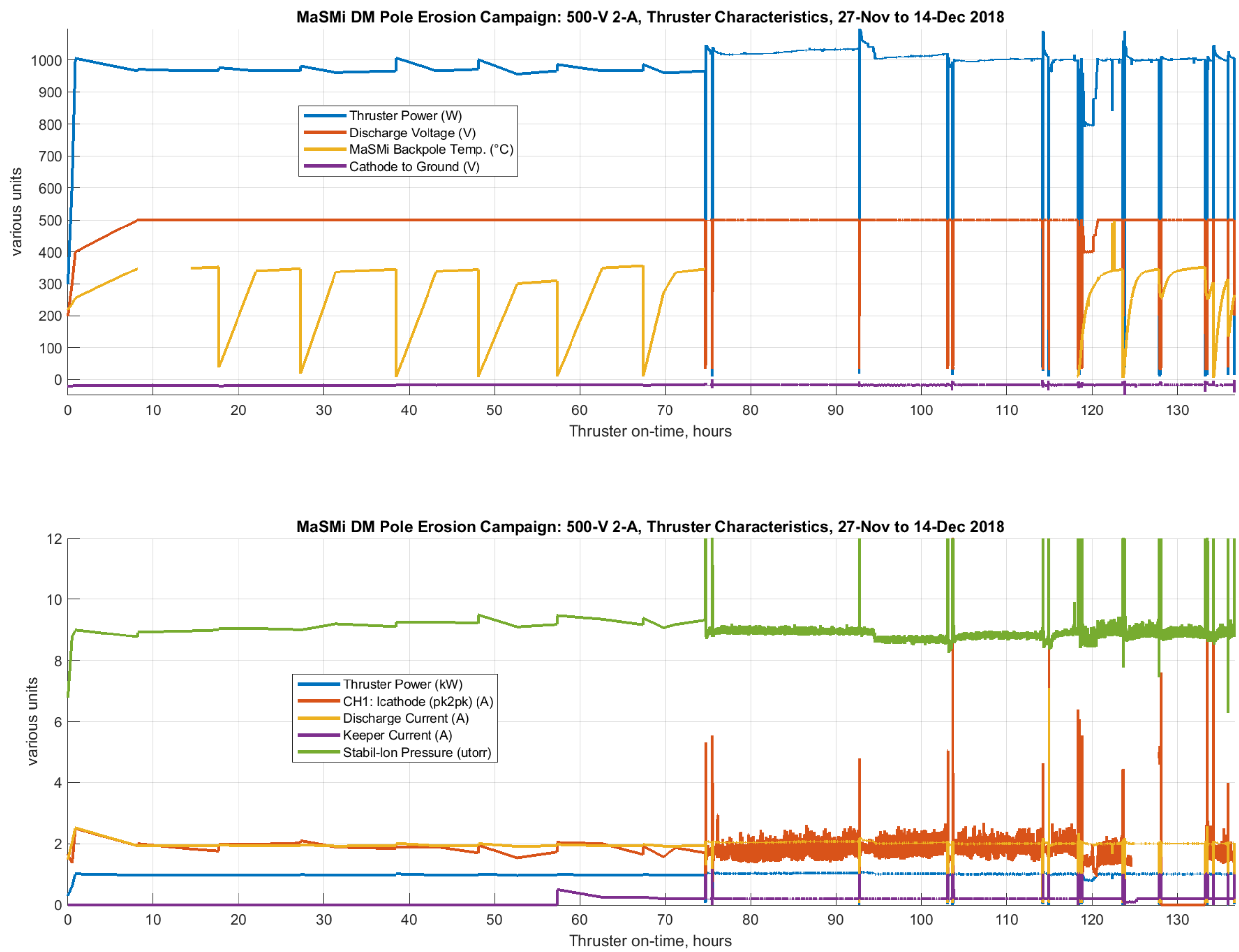

Figure 14. Various thruster telemetry signals versus thruster on-time for the highest power (1 kW) 500-V 2-A short duration wear segment.

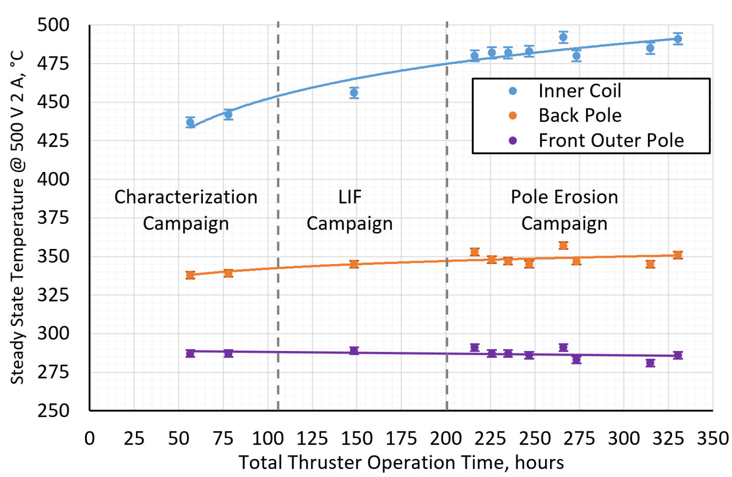

Figure 15. Longer term increase in inner coil steady state temperature observed in the operation of the MaSMi-DM thruster.

C. Steady-state temperature changes at the 500-V 2-A condition

While the steady-state backpole temperature seen in Figure 14 for the 500-V 2-A condition appears roughly invariant, a notable change was observed in the inner coil during the total hours run including MaSMi-DM characterization [18] and laser induced fluorescence [19] experiments pre-dating this pole erosion test campaign. In Figure 15, the gradual increase in inner coil steady-state 500-V 1000-W operating temperature is evident beginning at 437°C and leveling off at 491°C after 330 total hours of operation. It is plausible that the inner electromagnetic coil assembly may be more completely outgassed at this later point and may have less physical inter-coil material to assist in conductively pulling heat out of the thruster. It is also possible that the various stainless steel fasteners used to secure the inner coil assembly to the thruster may have loosened via creep or thermal cycling therefore increasing thermal resistance at these contacts and again limiting heat conduction out of the thruster. The design of the MaSMi-EM thruster uses an improved coil-to-thruster interface that mitigates this issue.

D. Thruster discharge oscillations and spectra throughout the test segments

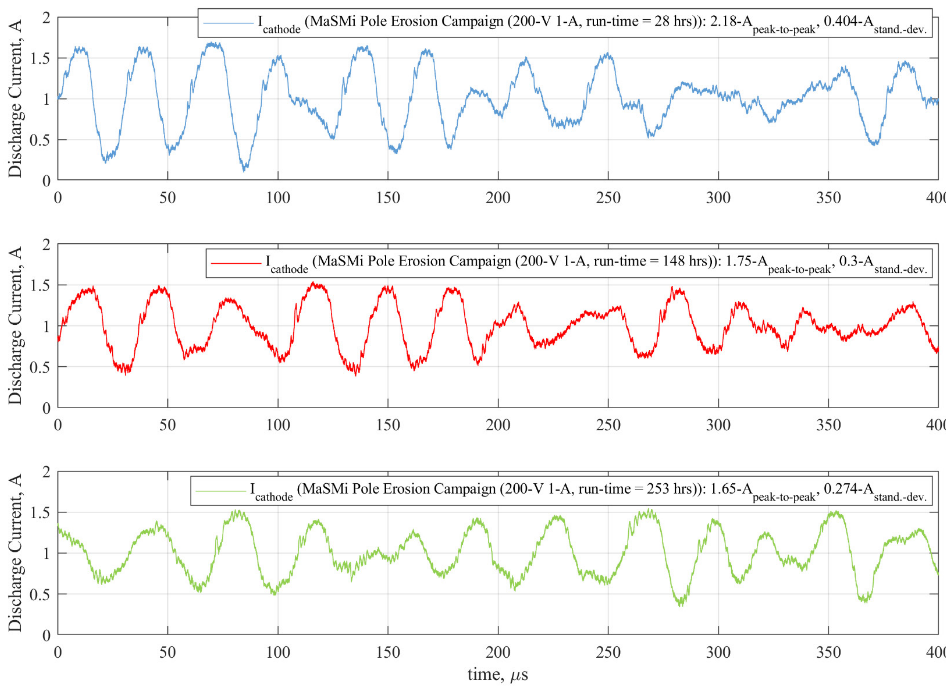

Figure 16. Time-series discharge current waveforms collected throughout the 200-V 1-A segment.

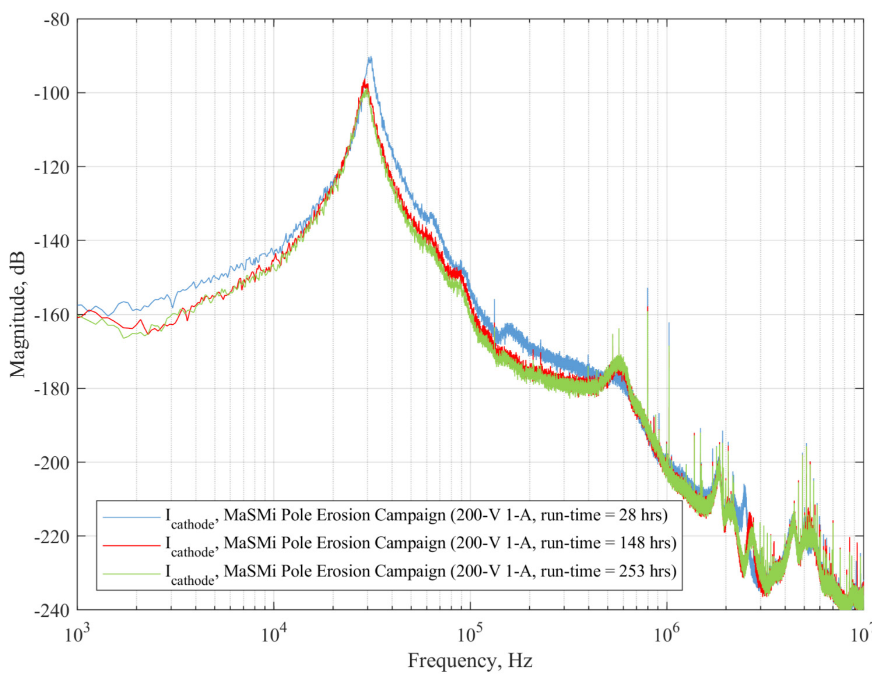

Figure 17. Discharge current oscillation spectra the throughout the 200-V 1-A segment.

Full (50 M element) scope traces were acquired throughout each of the short duration wear segments. For the 200-V 1-A segment, Figure 16 shows the time-series discharge current while Figure 17 shows the relative invariance in the various spectral features (e.g. the Hall thruster breathing mode at 30 kHz) of the discharge current signal. The 200-V 1-A segment did experience a 32% decrease in discharge current oscillation amplitude (see Figure 12) and this is observed as a decrease in the height of the main breathing mode peak—however the frequency of this peak at 30 kHz and the frequencies and amplitudes of higher frequency modes remained roughly constant.

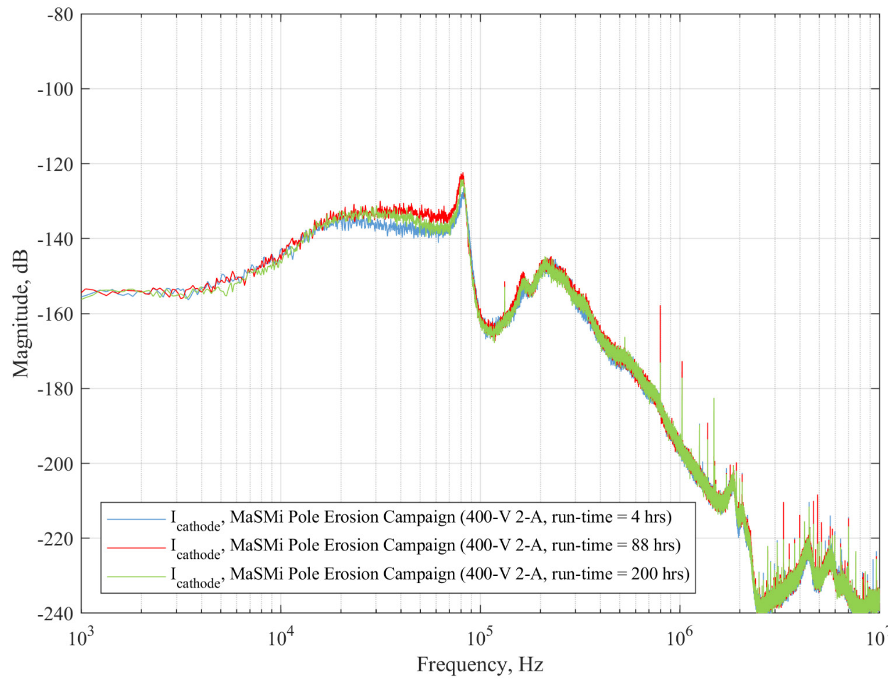

Figure 18. Discharge current oscillation spectra acquired throughout the 400-V 2-A segment.

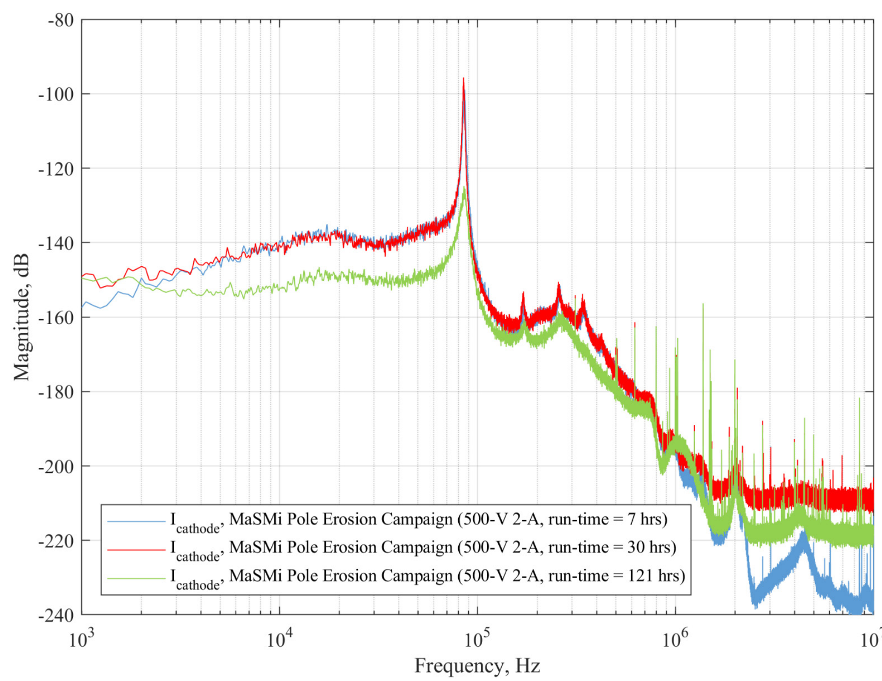

Figure 19. Discharge current oscillation spectra acquired throughout the 500-V 2-A segment. Note: the first two cases (7 h and 30 h) have a different discharge filter configuration.

Similar spectral invariance was observed for the other 400-v 2-A (Figure 18) and 500-V 2-A (Figure 19) test segments wherein the major peak frequencies and amplitudes remained approximately the same throughout the runtimes. This spectral invariance could have been predicted from the relatively constant discharge current oscillation amplitudes seen in Figure 13 (for the 400-V 2-A case) and Figure 14 (for the 500-V 2-A case). For the first two 500-V 2-A spectra acquired at 7 and 30 hours, the discharge filter was modified from Figure 4 with an additional cathode to ground capacitor. This capacitor was removed for all other cases, but it altered the spectra captured for these two datasets and prevented a 1:1 comparison of the spectra throughout the entire 500-V 2-A segment.

E. Pole erosion method of analysis

The method of determining the rate of pole erosion observed is relatively simple in that the step change in height from a region of the exposed pole cover is subtracted from a nearby region of the pole cover protected from a mask. This eroded depth is then divided by the total run time at this condition to compute the average erosion rate.[‡‡] It was known at the outset of this test campaign that the minimum resolvable erosion accuracy was ±1 μm (see section II.G). Early numerical simulations (newer more accurate simulations have since been performed [11]), estimated MaSMi pole cover erosion rates from ranging from 9 -170 μm/kh. This translated to total predicted erosion range of 2.3-43 μm during each of the planned 250 hour segments. Thus, it was deemed critical to maintain the ±1 μm accuracy of the height measurement in order to assess the lower end of the expected erosion. Just using the raw eroded profiles could not guarantee this ±1 μm accuracy since large-scale/global waviness was on the order of ±30 μm. Using local measurements reduced the impact of the waviness significantly. However, an improved approach was to use the uneroded pole cover scan to level correct the entire eroded scan. A special mounting fixture was used to ensure accurate alignment was retained after the pole covers were removed and then reinstalled following the each test segment. All scanning was performed in a clean room and the pole covers were lightly dusted using dry compressed N_2 gas. The mounting surface was also wiped clean with ethanol and dusted with compressed N_2 prior to each pole cover mounting. Finally, the mounting of the pole covers used screws torqued to the same level. Once this level correction was applied to the post-test segment pole cover scan, both the lower and upper edges of the mask were identified as lines in r-θ coordinates. 2D patches in r-θ space sized Δr by $\Delta\theta$ were then averaged under the mask (offset by $\theta_{mask\text{-}offset}$) and also averaged in the nearby exposed region of the pole cover (offset by $\theta_{exposed\text{-}offset}$). The averaging of these patches improved the signal to noise ratio of the measurement by eliminating for fine-scale surface roughness height variations. The size of the individual patches was selected provide ≳20 radially resolved points and to ensure only local measurements were used. The masked area offset, $\theta_{mask\text{-}offset}$=0.4°, was selected to ensure the patches remained under the mask and did not overlap with the mask screw hole. The exposed area offset, $\theta_{exposed\text{-}offset}$ =5°, was selected based on the observation that the region immediately next to the mask showed an uneven erosion profile. This likely arose from redeposition of sputtered material from the graphite mask edges back onto the exposed pole cover areas in close proximity to the mask edges. While only one radial profile of erosion was needed, the presence of two mask edges prompted the evaluation of the erosion seen at both the upper and lower mask edges.

‡‡ The measured carbon backsputter rate (see Section III.G) is then added to this step height change over time erosion rate to provide a corrected rate of erosion that would be realized in-flight.

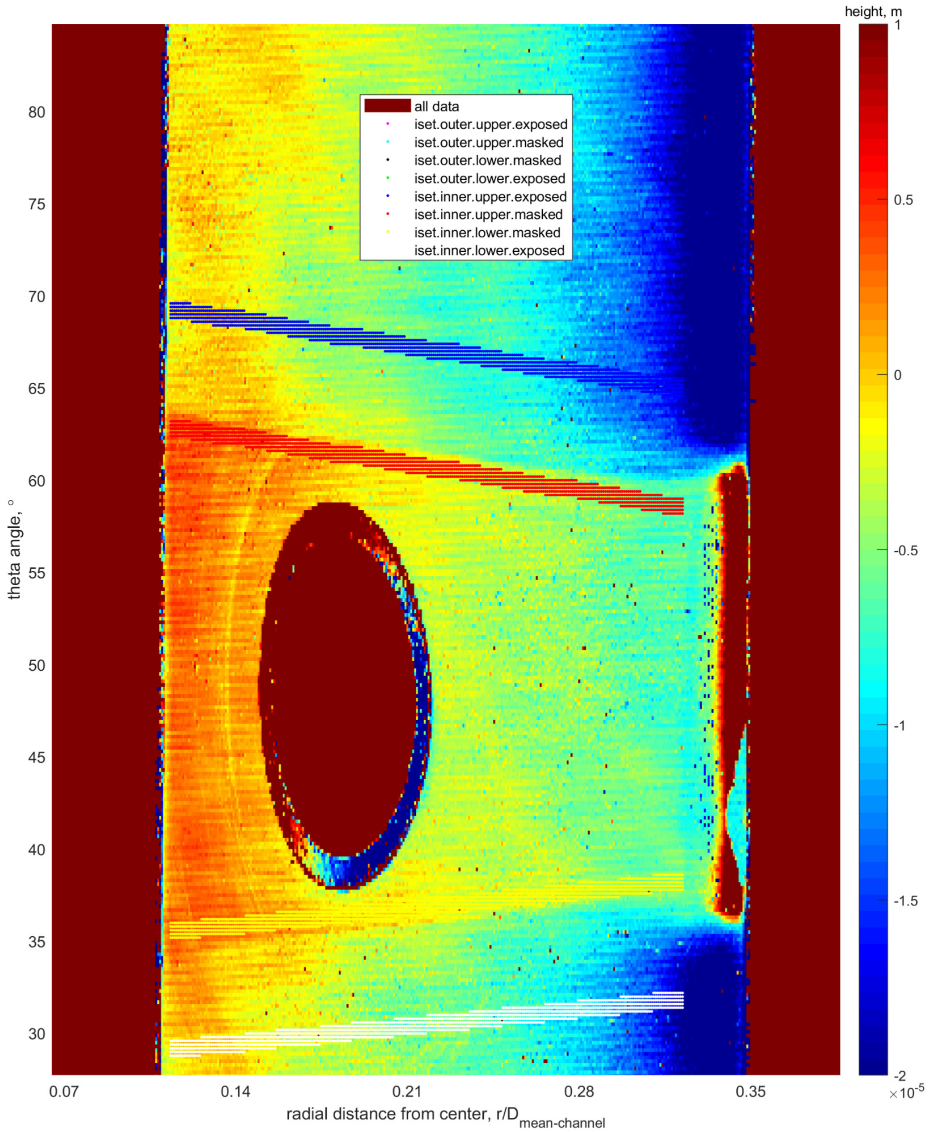

Figure 20. Processed inner-pole cover 3D scan in *r-θ* coordinates clearly showing the location of the mask as well as the 2D patches (colored markers) used to evaluate the step height change due the pole erosion of the unmasked portions of the pole cover.

A level corrected scan for the 200-V 1-A condition is shown in r-θ coordinates in Figure 20 with the 2D patches used to compute the erosion step height (between the mask covered and exposed regions) marked with "blue," "red," "yellow," and "white" markers. These same data are presented using more visually representative x-y coordinates in Figure 21. While the height data in each Δr by $\Delta\theta$ patch is generally smooth, occasional scan aberrations (or possibly small dust particles) exhibit spikes in the patch surface profile. To prevent these points form skewing the average height of the patch, any point exceeding 5 standard deviations is excluded from the averaging. The Nanovea profilometer uses the wavelength of the light *reflected* off the sample to determine the height. While the pre-test pole covers were smooth and highly reflective, the post-test pole covers were dull matte in appearance and reflected significantly less light. Indeed the post-test scan settings needed adjustment to ensure sufficient light signal reached the spectrometer detector. Even with these adjustments, some pixels still proved problematic. The spatial resolution of each raw pixel was on the order of 1 μm and it is plausible that occasionally the vertical edge of a surface roughness feature was imaged by the pixel providing zero back-reflected light. The profilometer can only scan vertical angles as steep as 87° for this reason.

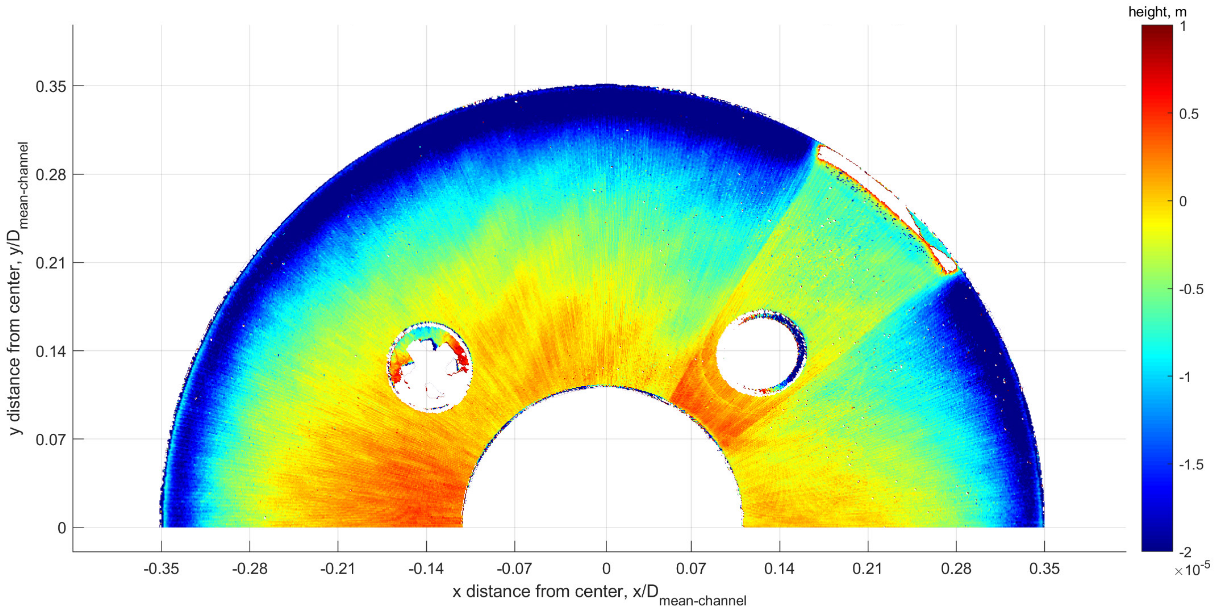

Figure 21. Processed inner-pole cover 3D scan in *x*-*y* coordinates clearly showing the location of the mask spanning approximately 1:00 to 2:00.

F. Pole erosion results

Using the proceeding method of analysis, the radially resolved erosion profile for the 200-V 1-A 253 hour wear segment is presented in Figure 22 including both the inner ($0.21 \leq r/\overline{r_{channel}} \leq 0.71$) and outer ($1.28 \leq r/\overline{r_{channel}} \leq 1.77$) graphite pole covers. Three erosion profiles are included for each pole cover including the erosion measured near the lower edge of the mask, near the upper edge of the mask, and the average of both locations. Notably, the erosion at the lower edge of the mask is consistently higher, suggesting that the eroding ions might have an azimuthal velocity component. The lower mask edge region would then be upstream of this azimuthal component and thus receive additional ion flux than the upper edge region that is shielded due to the finite height of the mask (0.65 mm thick). This seems plausible due to the azimuthally swirling Hall current in the nearby discharge channel. However, this azimuthal effect is small and largely falls inside the measurement uncertainty. Regardless, it seems prudent to consider the maximum of the erosion seen at both mask edges as the true erosion since it eliminates this possible mask shielding effect. The radial erosion rates for both the inner and outer pole covers rise dramatically near the discharge channel edges. This seems reasonable due to the higher plasma densities in these regions and the closer proximity to the acceleration zone and is consistent with prior observations from other magnetically shielded thrusters [12–14,16]. However, there is no significant increase in erosion near the cathode edge. The MaSMi-DM pole erosion profile for the 200-V 1-A segment also exhibits a several low-amplitude peaks and troughs that are observed consistently in both the lower and upper mask edge regions. The source of these radial features is unknown but—as they are roughly within the uncertainty—they can be ignored. Overall, the peak erosion rates are measured as 52.7 μm/kh for the inner pole cover ($\dot{h}_{inner-pole}$) and 47.4 μm/kh for outer pole cover ($\dot{h}_{outer-pole}$). The 1.5 mm thick pole covers would last approximately 28 kh at this 200-V 1-A operating condition (corresponding to >100 kg-Xe propellant throughput) if the entire thickness of the cover were to be eroded. However, it is possible that the erosion rates closer to the corners of the discharge channel (closer than was measured) are higher. Interpretation of the pole erosion 3D profilometer scans very near these edges was not feasible due to artifacts from the mask that corrupted the surface profile near the edge (see Figure 20 and Figure 21). Similar pole erosion studies with the HERMeS thruster [12–14] showed that the erosion often peaked before the edge of the pole cover near the discharge channel. Thus, it is also possible that MaSMi-DM pole cover erosion may actually decrease closer to the discharge channel edges. The modeled pole erosion rates for this condition also see a large increase (of about a factor of two, see Section III.H and Ref. [11]) very-near to the channel edges, however this peaked rate is only 72 μm/kh which is in family with the measured peak rate of 53 μm/kh.

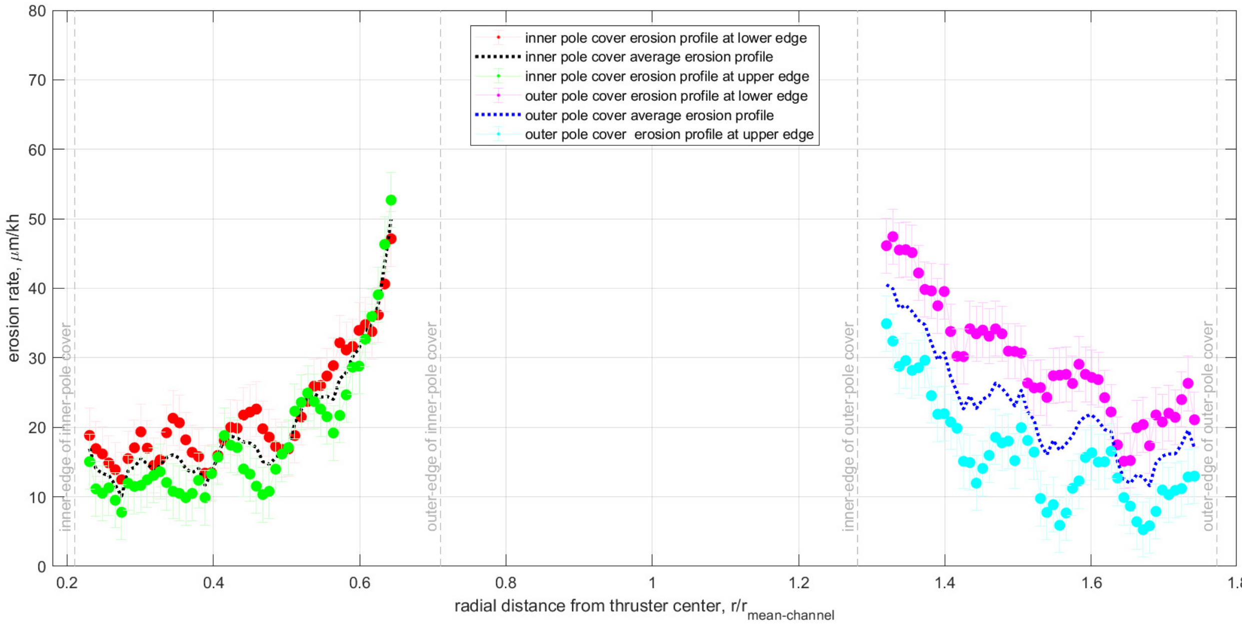

Figure 22. Radially resolved erosion rate profiles for the 200-V 1-A wear segment including the erosion rates measured near the lower and upper edges of the mask as well as the average erosion rate between these locations. The radial locations of the inner and outer pole cover edges are denoted.

Similar pole cover erosion profiles for the 400-V 2-A short duration wear test segment are presented in Figure 23. These profiles share many of the same characteristics as the prior 200-V 1-A condition albeit at a much lower overall peak erosion rates of 25 µm/kh (inner pole cover) and 16 µm/kh (outer pole cover). This higher power, 800-W, case was originally thought to produce higher erosion than the 200-W case. However, it is known from prior pole erosion numerical simulation efforts and experiments that thruster operating conditions with relatively large discharge oscillations that axially displace the acceleration zone can lead to larger rates of pole erosion [13]. The relative peak-to-peak over mean discharge current oscillation amplitudes compared to the maximum rates of pole erosion for the three tested segments are presented in Table 2.

Table 2. Peak-to-peak discharge current magnitudes and maximum pole cover erosion rates for all test conditions.

Condition	$\frac{I_{cathode,pk2pk}}{\overline{I_{cathode}}}$	$\dot{h}_{inner-pole}\big\|_{max}$	$\dot{h}_{outer-pole}\big\|_{max}$	Lifetime at condition§§	Propellant throughput at condition§§
200-V 1-A (200 W)	2.5 to 1.7	52.7 µm/kh	47.4 µm/kh	28,000 h	126 kg-Xe
400-V 2-A (800 W)	1.1	23.4 µm/kh	15.7 µm/kh	64,000 h	621 kg-Xe
500-V 2-A (1,000 W)	0.96	29.3 µm/kh	10.5 µm/kh	51,000 h	483 kg-Xe

This shows a clear correlation that increased oscillation amplitudes lead to increased rates of pole erosion. The current density is also lower for the more oscillatory and erosive 200-V 1-A condition but it is not clear if—or how—these properties are related. While the 400-V 2-A condition inner pole cover again shows increased erosion at radial location near the discharge channel the same is not necessarily observed with the outer pole cover. However, the very low rates of outer pole cover erosion (nearly within the uncertainty), may be hiding this trend. It is again observed that the lower edge regions of the inner and outer pole cover masks erode faster than the upper edges. This is again consistent with the theory of a counter-clockwise swirling azimuthal component to the eroding ion trajectories. Finally, the similar low-amplitude radial peaks and troughs are observed in the erosion rate profile as were seen in the 200-V 1-A condition.

§§ These are the predicted lifetimes and throughputs based solely on the measured rates of pole cover erosion and 1.5 mm pole cover thickness neglecting other potential life-limiting aspects of the thruster system such as fracturing of the graphite pole cover as it approaches zero thickness.

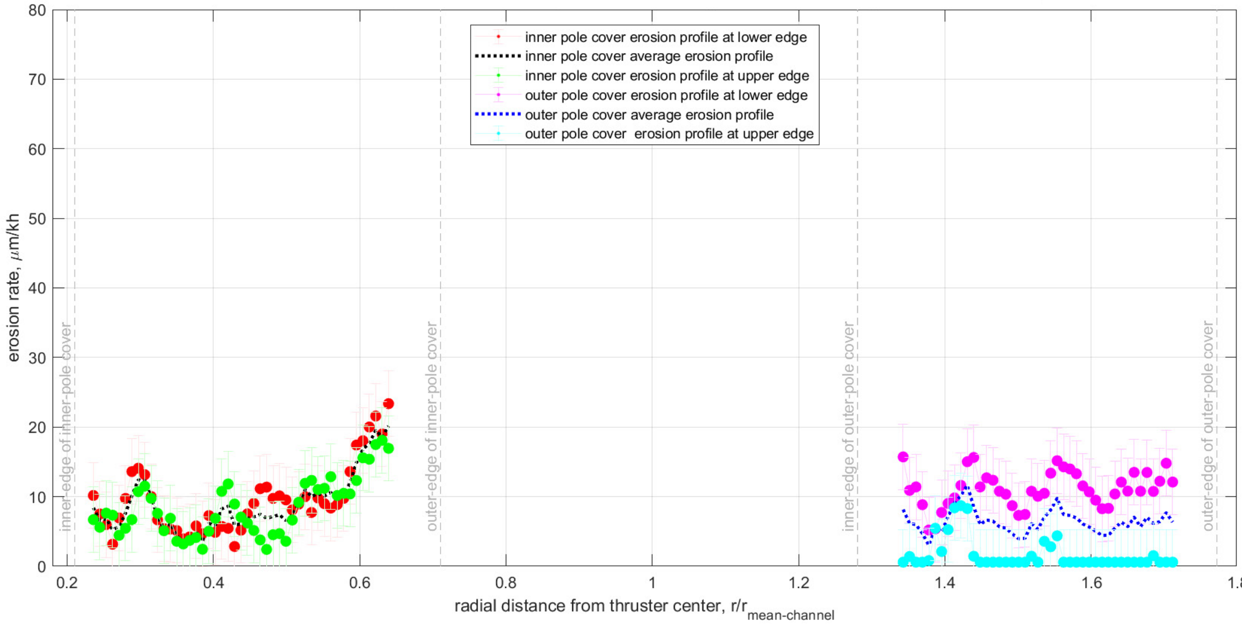

Figure 23. Radially resolved erosion rate profiles for the 400-V 2-A wear segment including the erosion rates measured near the lower and upper edges of the mask as well as the average erosion rate between these locations. The radial locations of the inner and outer pole cover edges are denoted.

The pole cover erosion rate profiles for the highest power, 1000 W, 500-V 2-A test segment are presented next in Figure 24. These erosion rate profiles closely match those seen at the prior 800-W condition with the exception that the outer pole cover erosion rates are nearly non-existent. While it is again surprising that the highest power highest voltage operating condition yields the lowest average rates of erosion, this condition was also the most quiescent with a peak-to-peak over mean discharge current amplitude averaging 0.96.

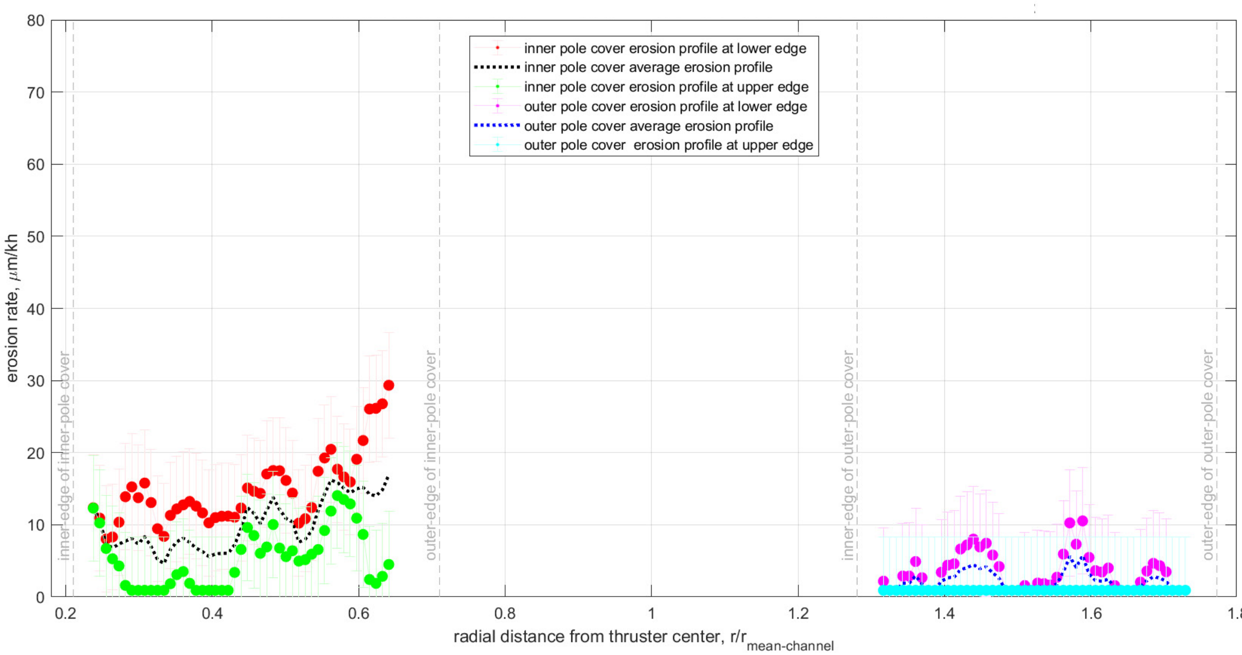

Figure 24. Radially resolved erosion rate profiles for the 500-V 1-A wear segment including the erosion rates measured near the lower and upper edges of the mask as well as the average erosion rate between these locations. The radial locations of the inner and outer pole cover edges are denoted.

For all three operating conditions, the pre-test and post-test mass differences for the inner and outer pole covers were also used to compute the average erosion rates. The presented erosion profiles (Figure 22 - Figure 24) were then integrated to compute average erosion rates that compared well to the mass loss estimated rates (within the uncertainty).

G. Facility backsputter rates and estimated channel wall erosion rates

The QCM was monitored regularly throughout the test campaign and Table 3 presents the average rates of backsputtered carbon throughout each of the short duration wear segments. While rates of carbon backsputter are relatively small, they have already been used to correct all the presented pole erosion rate data.‡‡ Indeed, since these backsputter rates are well inside the uncertainty of the pole erosion rate measurements (see Eq. (2)) this correction has a negligible effect. Otherwise, the rates of backsputter, $\dot{h}_{C-backsput.}$, follow the expected trend with thruster power that has been observed with other thrusters [25].

Table 3. QCM measured backsputtered carbon for each operating condition.

Condition	QCM total backsputter	QCM average backsputter rate, $\dot{h}_{C-backsput.}$
200-V 1-A (200 W)	0.05 μm	0.18 μm/kh
400-V 2-A (800 W)	0.13 μm	0.59 μm/kh
500-V 2-A (1,000 W)	0.12 μm	0.91 μm/kh

While these rates of backsputter are insignificant compared to all measured rates of pole cover erosion, they can be used to bound the maximum rates of discharge channel wall erosion that may exist in the absence of backsputtered carbon (e.g. in the flight environment). The gradual blackening of the discharge channel walls from the start to the conclusion of the pole erosion test campaign (shown in Figure 25) indicates that the net deposition of backsputtered carbon is exceeding any discharge channel wall erosion and enables an estimate (based on sputter yield ratios [2]) of discharge channel wall erosion of approximately $\dot{h}_{channel-erosion} \,\widetilde{\in}\, [\dot{h}_{C-backsput.}, 20 \cdot \dot{h}_{C-backsput.}]$. Thus, the maximum estimated rate of channel wall erosion could be as high 18 μm/kh which is orders of magnitude lower than unshielded thrusters (1,000-10,000 μm/kh is typical) and insignificant compared to the thickness of the discharge channel wall material.

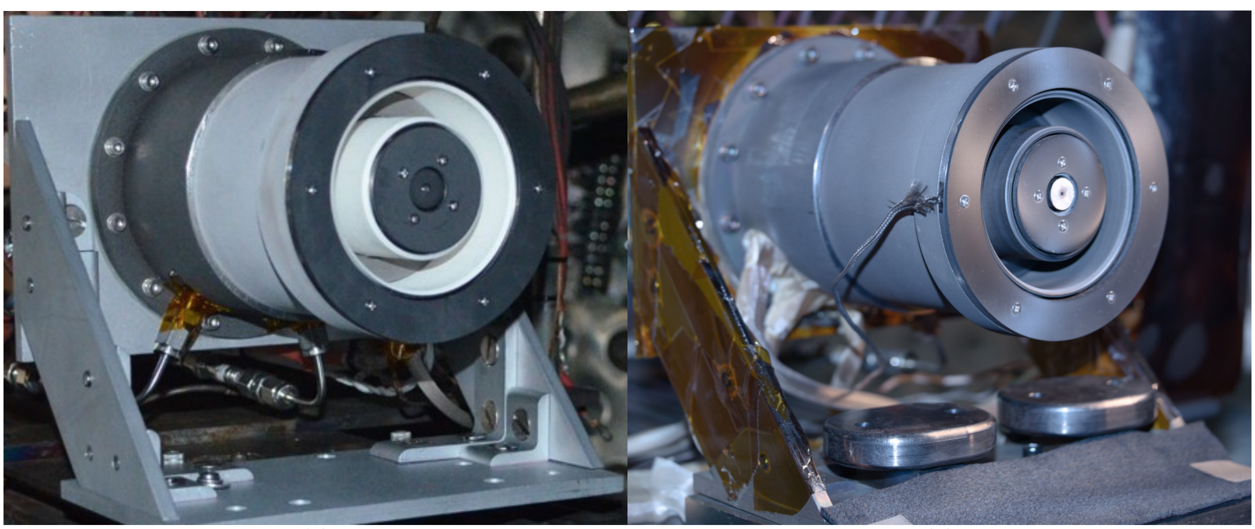

(a) (b)

Figure 25. Photographs of MaSMi-DM (a) prior to the start (0 h total runtime) and (b) after the conclusion of the pole erosion test campaign (approximately 800 h total runtime).

H. Measured versus simulated pole erosion rates

Comprehensive numerical simulations of the rate of pole erosion have been recently performed (see companion Ref. [11] for full details) and these roughly match the observed rates of erosion within a factor of 2 as shown in Figure 26 (average difference is 66%). Spikes in the erosion rates for all three conditions are predicted by the simulations right at the edges of the pole covers near the discharge channel. While this peak is only 72 μm/kh for

200 V 1 A, the simulated edge cover erosion peaks for 400 V 2 A and 500 V 2 A are 111 μm/kh and 141 μm/kh respectively. These higher simulated rates were not seen experimentally (23 μm/kh and 29 μm/kh maximums were measured at 400 V and 500 V respectively) but the experimental measurements were not performed right up to the pole cover edges. Regardless, this simulated peak in erosion is localized to the very-near corner and complete erosion of the pole cover at this location is not likely to affect thruster operation. Additionally, once a finite amount of near-edge pole cover erosion occurs, the new lowered effective location of the pole cover surface is likely to experience less erosion. The numerical simulations show that the pole erosion is caused by both beam ions as well as lower energy ions created downstream of the main acceleration zone. The low-energy ions comprise the bulk of the pole erosion seen in the 400-V 2-A and 500-V 2-A conditions with beam ions contributing only to the regions of the pole covers radially near the discharge channel. The 200-V 1-V condition however shows beam ions contributing to pole erosion across the entire pole cover faces as a result of transient beam divergence increases experienced during the large amplitude discharge current oscillations present. This effect leads to higher overall simulated erosion rates for this lowest power most oscillatory condition. The experimental data observed this same magnitude increase in erosion for this case providing confidence in the fidelity of the numerical simulations ability to predict pole erosion. However, one shortcoming of the present numerical simulations is that the magnitude of the discharge current oscillations and the location of the acceleration zone (using LIF data as in Ref. [19] for MaSMi) are required inputs from the experimental operation of the thruster.

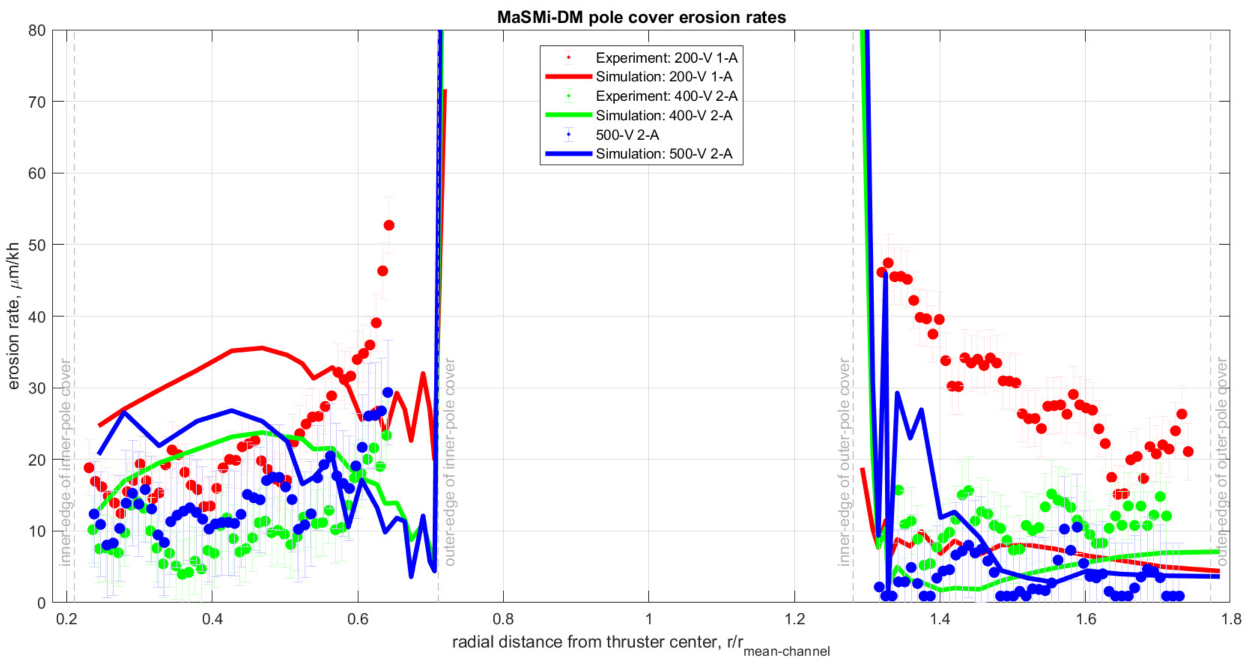

Figure 26. Experimental and simulated radially resolved erosion rate profiles for all short duration wear segments tested.

I. Observed pole cover fastener erosion

The stainless steel fasteners used to secure the pole covers to the poles of the MaSMi-DM were not designed to last the full predicted lifetime of the thruster (this design feature has been modified for the MaSMi-EM thrusters to exceed their 100-kg throughput lifetime requirement). Thus, these fasteners experienced significant erosion throughout the 805 hour total runtime of the MaSMi-DM thruster (including the characterization, LIF, and pole erosion campaigns). Measurements of the post-test lengths of the three inner pole cover fasteners (not including the fastener used to secure the mask) averaged 3.657 mm with ±6 μm standard deviation. Identical, but new fasteners averaged 3.755 mm (±14 μm standard deviation) in length. Thus, the overall rate of inner pole cover fastener erosion throughout all MaSMi-DM testing is shown in Eq. (3).

$$\overline{\dot{h}_{inner-polecover-fastener-erosion}} \approx \frac{(3755\ \mu m - 3657\ \mu m)}{0.805\ kh} = 122\ \mu m/kh \quad (3)$$

The sputter yield for iron is approximately 9 times that of graphite for 100-300 eV xenon ions [25], thus one might expect an average rate of graphite inner pole cover erosion on the order of 13.6 μm/kh at the radial location of the fasteners. Referring to pole cover erosion rates in Figure 22, Figure 23, and Figure 24, the average pole cover erosion rate near the inner fasteners is 11.8 μm/kh.

IV. Conclusion

A series of three short duration wear tests were conducted with the MaSMi-DM thruster at 200-V 1-A, 400-V 2-A, and 500-V 2-A to measure the rates of pole cover erosion. After corrections for the nearly negligible carbon backsputter rate, the maximum pole erosion rate of 53 μm/kh was seen at the lowest-power, but highest oscillation amplitude, 200-V 1-A condition. The higher power 400-V and 500-V conditions both exhibited pole cover erosion rates < 30 μm/kh. The current thickness of the graphite pole covers should provide a lifetime over 28,000 hours (or 126 kg-Xe throughput) before complete pole cover erosion occurs—well in excess of the MaSMi/ASTREAUS system propellant throughput requirement of 100 kg-Xe. Throughout the duration of each test segment (average duration was 200 h), the thruster telemetry including thrust, total efficiency, specific impulse, thruster temperatures, discharge oscillation spectra, facility pressure, and all other signals remained roughly invariant with two minor exceptions. During the highest power 500-V 1-kW segment, the maximum steady state operational temperature of the thruster inner coil rose about +54°C over the course of 330 hours of total operation—a possible effect of more fully outgassed electromagnetic coils or of loosening/creep of fasteners that increased thermal interface resistances. The only other notable change was a slight 32% decrease in the amplitude of the discharge current oscillations measured during the 253 h long 200-V 1-A segment. While the MaSMi-DM performed exceptionally well during this test campaign, lessons were learned that have resulted in design modifications for the MaSMi-EM thruster that is the baseline design for the ASTREAUS system. Some of the design improvements include: pole erosion tolerant pole cover fasteners, creepless internal fasteners, and a more robust anode manifold interface design (that mitigates the intermittent Paschen breakdown issues seen on the DM version). Finally, the overall rates of measured pole cover erosion agree decently with numerical simulations for the MaSMi-DM thruster providing further confidence that the ASTREAUS system will exceed its lifetime requirement for all operating conditions thereby providing future NASA SmallSat interplanetary missions with the highest-performance longest-lifetime sub-kW class Hall thruster developed to date.

Acknowledgments

The research described in this paper was carried out at the Jet Propulsion Laboratory, California Institute of Technology, under a contract with the National Aeronautics and Space Administration and funded through the internal Research and Technology Development program.

References

[1] Mikellides, I. G., Katz, I., Hofer, R. R., and Goebel, D. M., "Magnetic shielding of a laboratory Hall thruster. I. Theory and validation," *Journal of Applied Physics*, vol. 115, Jan. 2014, p. 043303.

[2] Hofer, R. R., Goebel, D. M., Mikellides, I. G., and Katz, I., "Magnetic shielding of a laboratory Hall thruster. II. Experiments," *Journal of Applied Physics*, vol. 115, Jan. 2014, p. 043304.

[3] Hofer, R. R., Kamhawi, H., Mikellides, I. G., Herman, Daniel, Polk, J. E., Huang, W., Yim, J., Myers, J., and Shastry, R., "Design Methodology and Scaling of the 12.5 kW HERMeS Hall Thruster for the Solar Electric Propulsion Technology Demonstration Mission," 62nd JANNAF Propulsion Meeting, Nashville, TN, June 1, 2015.

[4] Hofer, R. R., Polk, J. E., Sekerak, M. J., Mikellides, I. G., Kamhawi, H., Sarver-Verhey, T. R., Herman, D. A., and Williams, G., "The 12.5 kW Hall Effect Rocket with Magnetic Shielding (HERMeS) for the Asteroid Redirect Robotic Mission," AIAA 2016-4825, 52nd AIAA/SAE/ASEE Joint Propulsion Conference, July 22, 2016.

[5] Hofer, R. R., Cusson, S. E., Lobbia, R. B., and Gallimore, A. D., "The H9 Magnetically Shielded Hall Thruster," IEPC- 2017- 232, 35th International Electric Propulsion Conference, Atlanta, Georgia, USA, October 8, 2017.

[6] Cusson, S. E., Hofer, R. R., Lobbia, R. B., Jorns, B. A., and Gallimore, A. D., "Performance of the H9 Magnetically Shielded Hall Thrusters," IEPC- 2017- 239, 35th International Electric Propulsion Conference, October 8, 2017.

[7] Conversano, R. W., Goebel, D. M., Mikellides, I. G., Hofer, R. R., Matlock, T. S., Wirz, R. E., and Mikellides, I. G., "Magnetically Shielded Miniature Hall Thruster: Performance Assessment and Status Update," AIAA 2014-3896, 50th AIAA/ASME/SAE/ASEE Joint Propulsion Conference, July 25, 2014.

[8] Conversano, R. W., Goebel, D. M., Hofer, R. R., Mikellides, I. G., and Wirz, R. E., "Performance Analysis of a Low-Power Magnetically Shielded Hall Thruster: Experiments," *Journal of Propulsion and Power*, vol. 33, Apr. 2017, pp. 975–983.

[9] Conversano, R. W., Lobbia, R. B., Tilley, K. C., Goebel, D. M., Reilly, S. W., Mikellides, I. G., and Hofer, R. R., "Development and Initial Performance Testing of a Low-Power Magnetically Shielded Hall Thruster with an Internally-Mounted Hollow Cathode," IEPC-2017-064, 35th International Electric Propulsion Conference, Atlanta, Georgia, USA, October 8, 2017.

[10] Lopez Ortega, A., and Mikellides, I. G., "Investigations of Pole Erosion Mechanisms in the 12.5 kW HERMeS Hall Thruster with the Hall2De Code," AIAA 2018-4647, 2018 Joint Propulsion Conference, Cincinnati, Ohio, July 9, 2018.

[11] Lopez Ortega, A., Mikellides, I. G., Conversano, R. W., Lobbia, R. B., and Chaplin, V. H., "Plasma Simulations for the Assessment of Pole Erosion in the Magnetically Shielded Miniature Hall Thruster (MaSMi)," IEPC-2019-281, 36th International Electric Propulsion Conference, University of Vienna, Austria, September 15, 2019.

[12] Williams Jr, G. J., Kamhawi, H., Choi, M., Haag, T., Huang, Wensheng, Herman, D. A., Gilland, J. H., and Peterson, P. Y., "Wear Trends of the HERMeS Thruster as a Function of Throttle Point," IEPC-2017-207, 35th International Electric Propulsion Conference, October 8, 2017.

[13] Polk, J. E., Lobbia, R. B., Barriault, A., Chaplin, V. H., Lopez-Ortega, A., and Mikellides, I. G., "Inner Front Pole Erosion in the 12.5 kW HERMeS Hall Thruster Over a Range of Operating Conditions," IEPC-2017-409, 35th International Electric Propulsion Conference, Atlanta, Georgia, October 8, 2017.

[14] Frieman, J. D., Kamhawi, H., Williams, G., Huang, W., Herman, D. A., Peterson, P. Y., Gilland, J. H., and Hofer, R. R., "Long Duration Wear Test of the NASA HERMeS Hall Thruster," AIAA 2018-4645, 2018 Joint Propulsion Conference, July 8, 2018.

[15] Frieman, J. D., Kamhawi, H., Peterson, P. Y., Herman, D. A., Gilland, J. H., and Hofer, R. R., "Completion of the Long Duration Wear Test of the NASA HERMeS Hall Thruster," AIAA 201903895, AIAA Propulsion and Energy 2019 Forum, August 16, 2019.

[16] Sekerak, M. J., Hofer, R. R., Polk, J. E., Jorns, B. A., and Mikellides, I. G., "Wear Testing of a Magnetically Shielded Hall Thruster at 2000 s Specific Impulse," IEPC-2015-155, 34th International Electric Propulsion Conference, Kobe, Japan, July 6, 2015.

[17] Conversano, R. W., Barchowsky, A., Lobbia, R. B., Chaplin, V. H., Lopez Ortega, A., Loveland, J. A., Lui, A. D., Becatti, G., Reilly, S. W., Goebel, D. M., Snyder, J. S., Hofer, R. R., Randolph, T. M., Mikellides, I. G., Vorperian, V., Rapinchuk, J., Villalpando, C. Y., and Grebow, D., "Overview of the Ascendant Sub-kW Transcelestial Electric Propulsion System (ASTRAEUS)," IEPC-2019-282, 36th International Electric Propulsion Conference, University of Vienna, Austria, September 15, 2019.

[18] Conversano, R. W., Lobbia, R. B., Kerber, T. V., Tilley, K. C., Goebel, D. M., and Reilly, S. W., "Performance characterization of a low-power magnetically shielded Hall thruster with an internally-mounted hollow cathode," *Plasma Sources Science and Technology (in review)*, 2019.

[19] Chaplin, V. H., Conversano, R. W., Lopez Ortega, A., Mikellides, I. G., Lobbia, R. B., and Hofer, R. R., "Ion Velocity Measurements in the Magnetically Shielded Miniature Hall Thruster (MaSMi) Using Laser-Induced Fluorescence," IEPC-2019-531, 36th International Electric Propulsion Conference, University of Vienna, Austria, September 15, 2019.

[20] Dankanich, J. W., Walker, M., Swiatek, M. W., and Yim, J. T., "Recommended Practice for Pressure Measurement and Calculation of Effective Pumping Speed in Electric Propulsion Testing," *Journal of Propulsion and Power*, vol. 33, Aug. 2016, pp. 668–680.

[21] Polk, J. E., Pancotti, A., Haag, T., King, S., Walker, M., Blakely, J., and Ziemer, J., "Recommended Practice for Thrust Measurement in Electric Propulsion Testing," *Journal of Propulsion and Power*, vol. 33, Apr. 2017, pp. 539–555.

[22] Mackey, J., Frieman, J. D., Ahern, D. M., and Gilland, J. H., "Uncertainty in Electric Propulsion Erosion Measurements," AIAA 2019-3896, AIAA Propulsion and Energy 2019 Forum, August 16, 2019.

[23] Grys, K. de, Mathers, A., Welander, B., and Khayms, V., "Demonstration of 10,400 Hours of Operation on 4.5 kW Qualification Model Hall Thruster," AIAA 2010-6698, 46th AIAA/ASME/SAE/ASEE Joint Propulsion Conference & Exhibit, Nashville, TN, July 25, 2010.

[24] Hofer, R. R., Jorns, B. A., Polk, J. E., Mikellides, I. G., and Snyder, J. S., "Wear test of a magnetically shielded Hall thruster at 3000 seconds specific impulse," IEPC-2013-033, Presented at the 33rd International Electric Propulsion Conference, The George Washington University, Washington, D. C., October 6, 2013.

[25] Lobbia, R. B., Polk, J. E., Hofer, R. R., Chaplin, V. H., and Jorns, B., "Accelerating 23,000 hours of Ground Test Backsputtered Carbon on a Magnetically Shielded Hall Thruster," AIAA 2019-3898, AIAA Propulsion and Energy 2019 Forum, August 16, 2019.